Numerical and analytical modeling of flow partitioning in partially saturated fracture networks.

Jannes Kordilla[1], Alexandre M Tartakovsky[2], and Marco Dentz[3]

[1]University of Göttingen
[2]Pacific Northwest National Laboratory (DOE)
[3]IDAEA-CSIC

November 21, 2022

Abstract

Infiltration processes in fractured-porous media remain a crucial, yet not very well understood component of recharge and vulnerability assessment. Under partially-saturated conditions flows in fractures, percolating fracture networks and fault zones contribute to the fastest spectrum of infiltration velocities via preferential pathways. Specifically, the partitioning dynamics at fracture intersections determine the magnitude of flow fragmentation into vertical and horizontal components and hence the bulk flow velocity and dispersion of fracture networks. In this work we derive an analytical solution for the partitioning processes based on smoothed particle hydrodynamics simulations and laboratory studies. The developed transfer function allows to efficiently simulate flow through arbitrary long wide aperture fracture networks with simple cubic structure via linear response theory and convolution of a given input signal. We derive a non-dimensional bulk flow velocity ($\widetilde{v}$) and dispersion coefficient ($\widetilde{D}$) to characterize the system in terms of dimensionless horizontal and vertical time scales τ_m and τ_0. The dispersion coefficient is shown to strongly depend on the horizontal time scale and converges towards a constant value of 0.08 within reasonable ranges for the fluid and geometrical parameters, while the non-dimensional velocity exhibits a characteristic $\widetilde{v} \sim \tau_m^{-1/2}$ scaling. Given that hydraulic information is often only available at limited places within (fractured-porous) aquifer system, such as boreholes or springs, our study intends to provide a rudimentary analytical concept to potentially reconstruct internal fracture network geometries from external boundary information, e.g., the dispersive properties of discharge (groundwater level fluctuations).

Numerical and analytical modeling of flow partitioning in partially saturated fracture networks.

Jannes Kordilla[1], Marco Dentz[2], Alexandre M. Tartakovsky[3,4]

[1]University of Goettingen, Geoscientific Centre, Goettingen, Germany
[2]Institute of Environmental Assessment and Water Research (IDAEA), Spanish National Research Council (CSIC), Barcelona, Spain
[3]Department of Civil and Environmental Engineering, University of Illinois at Urbana-Champaign, Urbana, IL, USA
[4]Pacific Northwest National Laboratory, Richland, WA, USA

Key Points:

- Horizontal fractures control dispersion during infiltration events within vertical preferential pathway
- Partitioning dynamics at intersections control uptake and release from sub-vertical fractures
- An analytical solution is derived and the dynamics upscaled via convolution to obtain non-dimensional characteristics

Corresponding author: Jannes Kordilla, `jkordil@gwdg.de`

Abstract

Infiltration processes in fractured-porous media remain a crucial, yet not very well understood component of recharge and vulnerability assessment. Under partially-saturated conditions flows in fractures, percolating fracture networks, and fault zones contribute to the fastest spectrum of infiltration velocities via preferential pathways. Specifically, the partitioning dynamics at fracture intersections determine the magnitude of flow fragmentation into vertical and horizontal components and hence the bulk flow velocity and dispersion of fracture networks. In this work, we derive an approximate analytical solution for the partitioning process and validate it using smoothed particle hydrodynamics simulations and laboratory studies. The developed transfer function allows to efficiently simulate flow through fracture networks with simple cubic structure and arbitrary number of fractures and aperture sizes via linear response theory and convolution of a given input signal. We derive a non-dimensional bulk flow velocity ($\widetilde{v}$) and dispersion coefficient ($\widetilde{D}$) to characterize fracture networks in terms of dimensionless horizontal and vertical time scales τ_m and τ_0. The dispersion coefficient is shown to strongly depend on the horizontal time scale and converges towards a constant value of 0.08 within reasonable fluid and geometrical parameter ranges, while the non-dimensional velocity exhibits a characteristic $\widetilde{v} \sim \tau_m^{-1/2}$ scaling. Given that hydraulic information is often only available at limited places within (fractured-porous) aquifer system, such as boreholes or springs, our study intends to provide a rudimentary analytical concept to potentially reconstruct internal fracture network geometries from external boundary information, e.g., the dispersive properties of discharge (groundwater level fluctuations).

1 Introduction

Estimation of infiltration and recharge remains one of the most important challenges in modern hydrogeology (Scanlon & Cook, 2002; Scanlon et al., 2006) and is directly related to important topics such as integrated water resources management (Engelhardt et al., 2013; Alkhatib et al., 2019), safety of nuclear waste repositories (Bodvarsson et al., 1997; Tsang et al., 2015), and storage, release and degradation of nitrate and other agrochemical products (Ascott et al., 2016, 2017; Kurtzman et al., 2013; Wang et al., 2013). In contrast to the long-prevailing opinion that fractures (or, generally speaking, highly permeable heterogeneities embedded in porous media) do not transmit water under non-equilibrium conditions due to the strong capillary forces in the adjacent matrix

(Singhal & Gupta, 2010), arrival times recorded in field and laboratory experiments strongly suggest the existence of rapid preferential flow along fractures, fracture networks, and fault zones (Zhou et al., 2006; Dahan et al., 2000; Weisbrod et al., 2000). The dynamic activation of preferential flow domains within the vadose zone controls the short- and long term hydraulic response of the groundwater to precipitation signals (Nimmo & Perkins, 2018) and hence affects the magnitude and temporal distribution of recharge. This is even more critical given the current predictions of climate-change-induced erratic and potentially extreme precipitation patterns (Black, 2009) that require precise estimation and management of limited recharge volumes, even more so in systems with thick vadose zones (Dvory et al., 2016; El-Hakim & Bakalowicz, 2007).

Despite the importance of the vadose zone for infiltration processes, both with respect to volumetric extent and share of the total aquifer volume, modeling approaches often do not (and can not due to missing information) consider the complexity of fractured-porous media to model the delay in arrival times and hence dispersion of an input signal. The complexity arises from geological heterogeneities that provide continuous pathways on various scales for rapid percolation and transport within fractures. In karst systems, precipitation is commonly partitioned into diffuse and preferential components, where the latter is commonly linked to direct infiltration in the surrounding area of surface depressions, dry valleys and dolines (Kordilla et al., 2012; Williams, 2008; Sauter, 1992; Gunn, 1981). Fault zones may cut across several geological units and provide catchment scale preferential flow paths in the form of strongly connected clusters of fractures (Bodvarsson et al., 1997; Flint et al., 2001; H. H. Liu et al., 2004). Tectonically induced stress fields and stress field changes generally promote the formation of local discontinuities, such as fractures, joints and fault zones in consolidated porous rocks (Ford & Williams, 2013; Neslon, 2001). What sets such features apart from typical pore space geometries is their strong anisotropic character, i.e., their length or spatial extent is orders of magnitude larger than their aperture. When fractures are connected, they can form percolating clusters (Berkowitz & Scher, 1995; Adler et al., 2013) that can reach length scales far beyond the thickness of individual geological layers/units and potentially extend across the entire vadose zone. Similar features can be observed in soil systems, a type of material the heterogeneity is commonly associated with macropores (wormholes), which can also form percolating clusters (Jarvis, 1998; Hussain et al., 2019; Nimmo, 2010).

Assessing recharge dynamics in fractured-porous systems on the field scale is difficult (Scanlon & Cook, 2002). Phreatic zone techniques assess recharge at the water table or at springs (e.g., tracers, water table fluctuations, Cook & Solomon, 1997; Nimmo & Perkins, 2018), hence, the estimates can potentially reflect catchment scale dynamics or at least sub-catchment recharge processes within the hydraulic influence area of the measurement point. In contrast, vadose zone techniques rely on measurements above the groundwater table, (e.g., lysimeters, Darcy's law, tracers, Heppner et al., 2007; Rossman et al., 2014; Chambers et al., 2019). They allow a rather localized quantification of recharge or water content and only integrate a limited volume above the point of measurement as infiltration commonly occurs nearly vertical. As most of these methods rely on rather simple assumptions about the internal systems geometry and percolation processes, the predictive power and temporal resolution is often limited (Scanlon & Cook, 2002).

In order to shed light on the complex infiltration processes, laboratory scale experiments have been a promising addition to the former investigation methods as they allow to isolate important processes under well controlled conditions that are often impossible to observe in-situ. Small-scale laboratory experiments for gravity-driven partially-saturated flow often exhibit erratic or chaotic flow dynamics (Su et al., 2001; Dragila & Weisbrod, 2004; Nicholl & Glass, 2005; T. Wood & Huang, 2015). In general, flow modes on the wall of wide fractures evolve with increasing flow rates from thin adsorbed films to droplets and rivulets to wavy surface films (Jones et al., 2017; Dippenaar & Van Rooy, 2016; Dragila & Wheatcraft, 2001; Ghezzehei, 2004). Different flow modes may also coexist. Consequently, experimental results are difficult to cast into meaningful frameworks. This especially concerns the complex flow dynamics at fracture intersections, which act as critical relay points controlling: (1) the overall connectivity of fracture networks (Adler et al., 2013); (2) the flow partitioning dynamics between connected fracture elements (Xue et al., 2020; Yang et al., 2019; Dragila & Weisbrod, 2004); and, ultimately, (3) the distribution of flow modes on fracture surfaces (Dippenaar & Van Rooy, 2016; Jones et al., 2017; Shigorina et al., 2019), which, in turn, can affect the interaction between porous matrix and fracture (Tokunaga & Wan, 1997; Tokunaga, 2009). Here, the term "partitioning" refers to the process of fluid redistribution at a fracture intersection, which depends on the relation between capillary, inertial, and viscous forces (Nicholl & Glass, 2005) and complexities such as velocity-dependent contact angles (Xue et al., 2020; Yang et al., 2019).

In terms of fracture aperture, numerical and laboratory studies of unsaturated flow in fractures have covered various length scales, from sub-millimeter scales (Glass et al., 2003; Ji et al., 2004, 2006; Nicholl & Glass, 2005), over ranges close to the capillary-inertial transition around 0.7mm (T. R. Wood et al., 2002, 2005), to apertures well within the inertial-dominated regime (Tokunaga & Wan, 1997, 2001; Dragila & Weisbrod, 2004; Tartakovsky & Meakin, 2005a, 2005b; Huang et al., 2005; M. Liu et al., 2007). Studies of free surface flow on a fracture plane without an intersection have been conducted by Shigorina et al. (2019); Kordilla et al. (2013); Hayden et al. (2012); Ghezzehei (2004).

Depending on the experimental setup, studies have focused either on the partitioning process at fracture intersections (Dragila & Weisbrod, 2004) or the (long-term) bulk system response (Ebel & Nimmo, 2013; Nimmo, 2010), which both form an integral part of understanding preferential flow dynamics through fractured systems. For the former case, a single fracture intersection of a horizontal and a vertical fracture is often "constructed", for example, by breaking glass plates, which results in a quasi-two-dimensional setup (Ji et al., 2006). Modifications to this setup include experiments with a slight offset at the fracture intersection or T-shaped intersections at various degrees of rotation (T. R. Wood et al., 2005; Xue et al., 2020; Yang et al., 2019). Intersections resembling an inverted Y-structure have been studied for example by Dragila and Weisbrod (2004), M. Liu et al. (2007) and Tartakovsky and Meakin (2005a). The combination of several, commonly cross-shaped, fracture intersections allows to study flow convergence, i.e., the deviation from classical volume-effective diffusive flow dynamics, typical for non-fracture porous media. Studies of this kind have been conducted by T. R. Wood et al. (2002, 2005); T. Wood and Huang (2015); Glass et al. (2003); LaViolette et al. (2003), often reaching timescales of several minutes or days. In the study by Glass et al. (2003), fractures are embedded into an impermeable matrix, while the other authors constructed their fracture networks from geological materials. Incorporation of the porous matrix can be considered another important classification parameter of fracture-scale studies. For large-aperture fractures, i.e., inertial-dominated flow systems that limit the contact time between fracture flow and matrix flow and/or a low-permeable matrix, the effect of matrix storage may be neglected. This can be observed in fractured karst systems, where fractures are often enlarged by dissolution (Dijk et al., 2002; Benson, 2001) or fractured crystalline rocks with extremely low matrix porosity and a severely limited advective potential.

Despite these research efforts the gap between small-scale process understanding and larger-scale application is still limited. In our recent work (Noffz et al., 2018), we demonstrated how to model breakthrough behavior in terms of discharge at the bottom of arbitrary long stacks of sugar-cube fracture arrays (Barenblatt et al., 1960) via linear response theory and convolution of input signals, whereas the transfer function has been obtained empirically for a given setup of a wide aperture vertical surface intersected by a horizontal one. However, it is desirable to obtain the form of the transfer function a priori using information about the internal geometry as well as fluid properties and fluid-solid interaction characteristics. Therefore, in this work, we provide an analytical solution for the transfer function and validate it using numerical simulations. The analytical solution describes the horizontal fracture infiltration until critical pressure thresholds trigger the breakthrough and dynamics are governed by Washburn-type flows and is conceptually based on the numerical studies and former laboratory studies (Noffz et al., 2018). Vertical flows are approximated by a film flow model. Finally, we employ linear response theory to model flow through arbitrary numbers of fracture intersections with explicit geometry and derive non-dimensional dispersion and velocity parameters ($\widetilde{D}$,$\widetilde{v}$) that depend on the dimensionless horizontal and vertical fracture time scales (τ_m,τ_0). Flows are shown to converge to a near-constant dispersion coefficient with increasing τ_m, while non-dimensional velocities scale as $\widetilde{v} \sim \tau_m^{-1/2}$ within feasible critical Reynolds number ranges.

2 SPH model for simulating flow in fracture networks

We use a two-dimensional SPH model to analyze complex flow partitioning at fracture intersections. SPH is a Lagrangian meshless method able to simulate complex flows with highly dynamic interfaces and is especially suited for the simulation of free-surface (pseudo-multiphase) liquid flows with continuous gas phase, effects of surface tension, and static/dynamic contact angles. We use a two-dimensional version of the massively parallel three-dimensional code of (Kordilla et al., 2017) that has been extended with an alternative formulation of the no-slip boundary condition. A detailed description of the SPH free flow model and its implementation in a parallel code, the reader is referred to Kordilla et al. (2017) and references therein. The SPH equations are summarized in Appendix A.

Here, we validate the SPH code for two classical static and dynamic flow cases that are related to the processes encountered in our application of flow in fractures, Poiseuille flow in a parallel plate system and capillary rise in a vertical tube.

2.1 Poiseuille Flow

In this section we demonstrate that for sufficiently large values of the friction coefficient β in the SPH momentum conservation equations (A3) and (A6), the SPH method recovers the solution of the NS equations subject to no-slip boundary condition at the fluid-solid boundary. Specifically, we use the SPH code with β ranging from 1×10^{-1} to $1 \times 10^{2}\,\mathrm{kg\,m^2s^{-1}}$ to simulate a two-dimensional Poiseuille flow problem and validate the SPH solutions for velocity against the analytical solution for the no-slip boundary condition (Sigalotti et al., 2003)

$$v_x(y,t) = \frac{\mathbf{g}}{2\nu}(y^2 - d^2) + \sum_{0}^{\infty} \frac{16(-1)^n d^2 \mathbf{g}}{\nu \pi^3 (2n+1)^3} \cos\left[\frac{(2n+1)\pi y}{2d}\right] \exp\left[-\frac{(2n+1)^2 \pi^2 \nu t}{4d^2}\right], \quad (1)$$

where the center is located at $y = 0$, $d = L/2$ such that the solid boundaries are located at $y = \pm d$.

Flow is simulated using the following parameter set: The inter-particle spacing is $\Delta x = 2 \times 10^{-5}\,\mathrm{m}$, $L = 200\Delta x = 5 \times 10^{-5}\,\mathrm{m}$, $\rho = 1000\,\mathrm{kg\,m^{-3}}$, $\mu = 1.25 \times 10^{-3}\,\mathrm{kg\,m^{-1}\,s^{-1}}$ and a body force of $g = 1.25 \times 10^{-5}\,\mathrm{m\,s^{-2}}$ is applied parallel to the x-direction. Five layers of boundary particles are placed at $y = 0$ and $y = L$ to ensure kernel consistency. For the given parameter set this yields a Reynolds number of $Re = \frac{v_x^\infty L \rho}{\mu} = 1.0$, where v_x^∞ is the maximum steady-state velocity.

Results indicate that the SPH solution converges to the exact no-slip solution for $\beta > 10$ (which corresponds to the artificial slip length $\lambda < L/100$) with an error on the order of 1.5% or lower. This holds for all time steps during the initial acceleration of the fluid within the capillary.

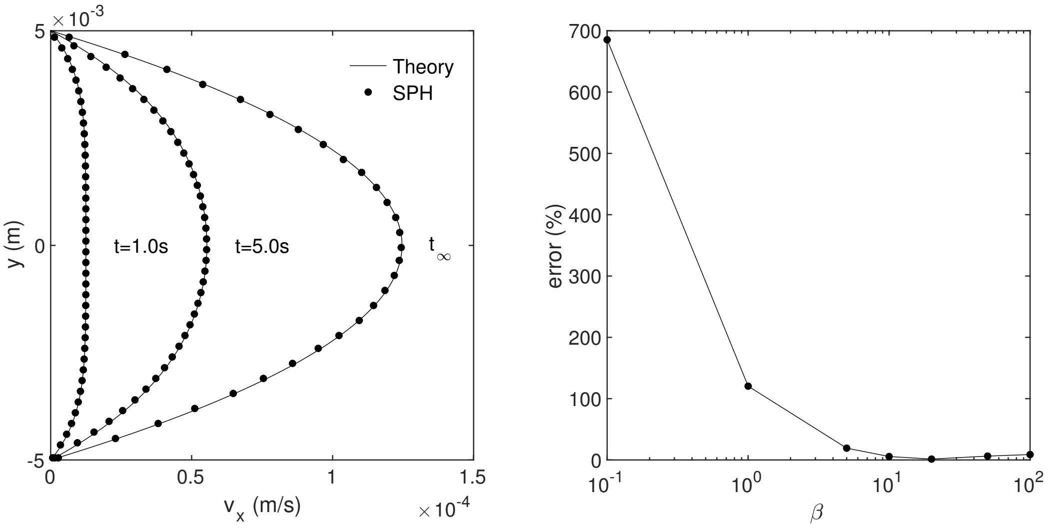

Figure 1. Comparison of the SPH model with the time-dependent solution for Poiseuille flow in a parallel plate system. The right figure shows the absolute percentage error which is below ≈1.5% for sufficiently large β (> 10), i.e., proper no-slip conditions.

2.2 Capillary Rise in a Tube

Here we simulate capillary rise in tubes of varying radius and compare the equilibrium fluid column height to the classical theory of Jurin (1718) and extended theories of Legait and de Gennes (1984) and Barozzi and Angeli (2014).

The classical theory of capillary rise is based on the parallel plate concept:

$$\frac{dh}{dt} = \frac{\Delta P}{h(t)} \frac{(2r)^2}{12\mu} \tag{2}$$

Here r is the radius of the fracture, and h the height of the triple contact line from the water surface. The total pressure in a two-dimensional systems consists of the capillary pressure and the pressure due to the weight of the water column

$$P_c^{2D} = \frac{\sigma cos(\theta_0)}{r} \qquad\qquad P_h = \Delta P g h(t) \tag{3}$$

Plugging the total pressure $\Delta P = \Delta P_c^{2D} - P_h$ into Eq. 2 and for $dh/dt = 0$ the maximum rise becomes:

$$\Delta h = \frac{\sigma cos(\theta_0)}{r\rho g} \tag{4}$$

As the curvature of the meniscus slightly depends on h a common extension of Eq. 4 is given by (Legait & de Gennes, 1984) as:

$$\Delta h = \frac{1 - \kappa^2 r^2 0.175}{\kappa^2 r} \qquad \kappa = \left(\frac{\rho g}{\sigma cos(\theta_0)} \right)^{1/2} \tag{5}$$

Barozzi and Angeli (2014) extend the solution by adding a correction term that accounts for the additional fluid volume over the apex of the meniscus

$$\Delta h = \frac{\sigma cos(\theta_0)}{r \rho g} - \frac{r}{3cos(\theta)} \tag{6}$$

The SPH simulations are run with an inter-particle spacing of $\Delta x = 5 \times 10^{-5}$ m, a density of $\rho = 1000\,\mathrm{kg\,m^{-3}}$ and a body force of $g = 9.81\,\mathrm{m\,s^{-2}}$ applied in normal direction to the bottom boundary. The viscosity is $\mu = 0.001\,\mathrm{kg\,m^{-1}s^{-1}}$ and the no-slip condition is enforced with $\beta = 25$. The speed of sound is set to $c_0 = 3\,\mathrm{m\,s^{-1}}$. Interaction forces are set to $s_{sf} = 0.015$ and $s_{ff} = 0.02$, which yields a surface tension of $\sigma = 0.0742\,\mathrm{kg\,s^{-2}}$ and a static contact angle of $\theta_0 = 69°$. The domain has a width of $L_x = 800\Delta x = 4.0\,\mathrm{cm}$. The height of the capillary is $L_y = 340\Delta x = 1.7\,\mathrm{cm}$ and is placed $\Delta L_y = 60\Delta x = 3\,\mathrm{mm}$ above the bottom boundary. Mirror boundaries are applied in x-direction. All solid boundaries are five particles thick to ensure kernel consistency. Simulation are initiated with a flat fluid surface covering the domain with an initial height of $145\Delta x = 7.25\,\mathrm{mm}$. The aperture of the capillary is varied in a range of 1.5 mm to 3.5 mm.

Simulations are run until an equilibrium is established and the maximum height is reached within the capillary. In order to measure Δh we determine the minimum height h_{min} of the fluid as the average of the water height $20\Delta x$ away from the left and right mirror boundary (see Fig. 2). The maximum height h_{max} of the fluid column is measured at the outer part of the capillary meniscus and hence we obtain $\Delta h = h_{max} - h_{min}$. The contact angles at equilibrium are obtained from a circle fit using the Pratt method (Pratt, 1987)(Fig. 3, left).

Results of the SPH simulations and theoretical results are shown in Fig. 3. Numerical results are in good agreement with the theoretical predictions and lie in between the predictions of Jurin (1718), Legait and de Gennes (1984) and Barozzi and Angeli (2014).

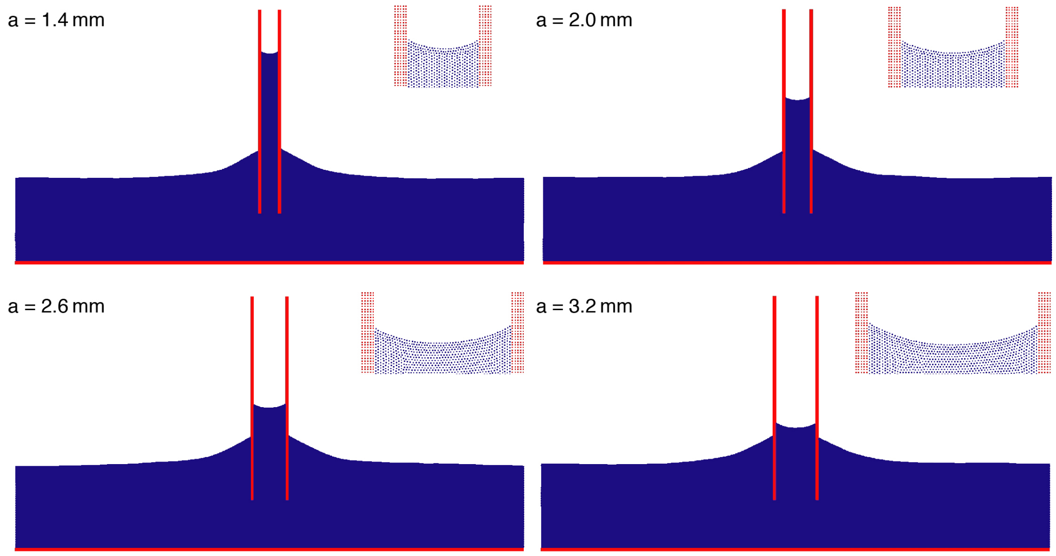

Figure 2. 2D simulations of capillary rise shown at steady-state conditions. The insets show the upper fluid front. The height of the capillary is $L_c = 1.7\,\text{cm}$, the width of the domain is $L_w = 4.0\,\text{cm}$ with periodic boundary conditions in the x-direction.

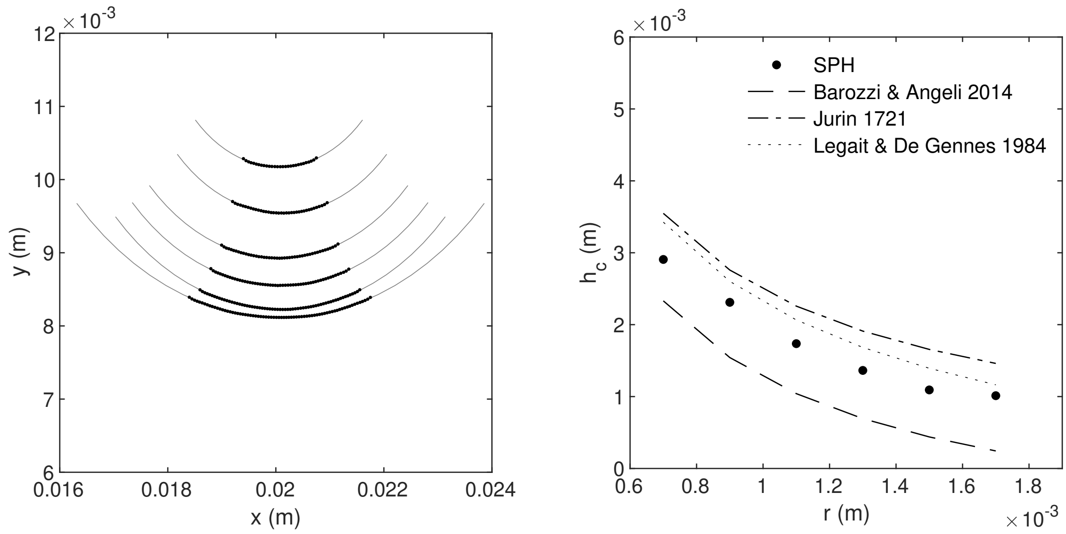

Figure 3. (Left) Fluid-air interfaces for all capillary sizes and the respective circle fit using the Pratt method. (Right) Theoretical predictions of the capillary rise h_c are plotted using the average contact angle of all simulations.

3 Results and Discussion

In the following subsections we (1) conceptualize the flow partitioning at a T-type fracture intersection, (2) derive an analytical transfer function for the partitioning including fluid movement on the vertical surfaces, (3) provide an upscaling solution via convolution and linear response theory, and finally (4) derive expression for arrival times and bulk dispersion that are then (5) analyzed in non-dimensional form to provide a comprehensive picture of the larger scale infiltration dynamics and its relation to the internal geometry.

3.1 Rivulet flow partitioning at a fracture intersection

In this section we derive a solution for the partitioning dynamics of rivulet flow down a vertical plane intersected by a horizontal smooth fracture (see Fig. 4) and compare it to our SPH model results. We consider the threshold at which critical capillary pressures within the horizontal fracture are high enough to route flow further down onto the vertical surface. At this point flow in the horizontal fracture transitions from a linear plug-flow type into a Washburn-type flow regime.

The flow rate $Q_h(t)$ (m^2s^{-1}) in the horizontal fracture is approximately given by the Darcy law:

$$Q_h(t) = \frac{k(P_{in}(t) - P_f)}{\mu l(t)}\,, \tag{7}$$

where t is time from the moment water entered the horizontal fracture, $k = a^2/12$ (m^2), a is the aperture (m), μ is the viscosity, P_f and $P_{in}(t)$ are the pressures at the invading front (point 1 in Fig. 4(1)) and the horizontal fracture entrance (point 2 in Fig. 4(1)), respectively, and $l(t)$ is the distance from the front to the fracture entrance.

From the Young-Laplace law, the pressure at the invading front is

$$P_f = P_{air} - \frac{\sigma}{R} = P_{air} - \sigma\frac{2\cos(\theta)}{a}, \tag{8}$$

where σ is the surface water-air surface tension, P_{air} is the air pressure, and $R = \frac{a}{2\cos\theta}$ is the front curvature, and θ is the contact angle.

Initially, all flow in the vertical fracture is diverted to (imbibed into) the horizontal fracture, i.e., $Q_h(t) = Q_0$, as shown in Fig. 4(1). Later, flow partitions, i.e., flow is both penetrating the horizontal fracture and flowing down the wall of the vertical fracture segment, as depicted in Fig. 4(2). When flow is partitioned, $P_{in}(t) = P_{air}$ (point

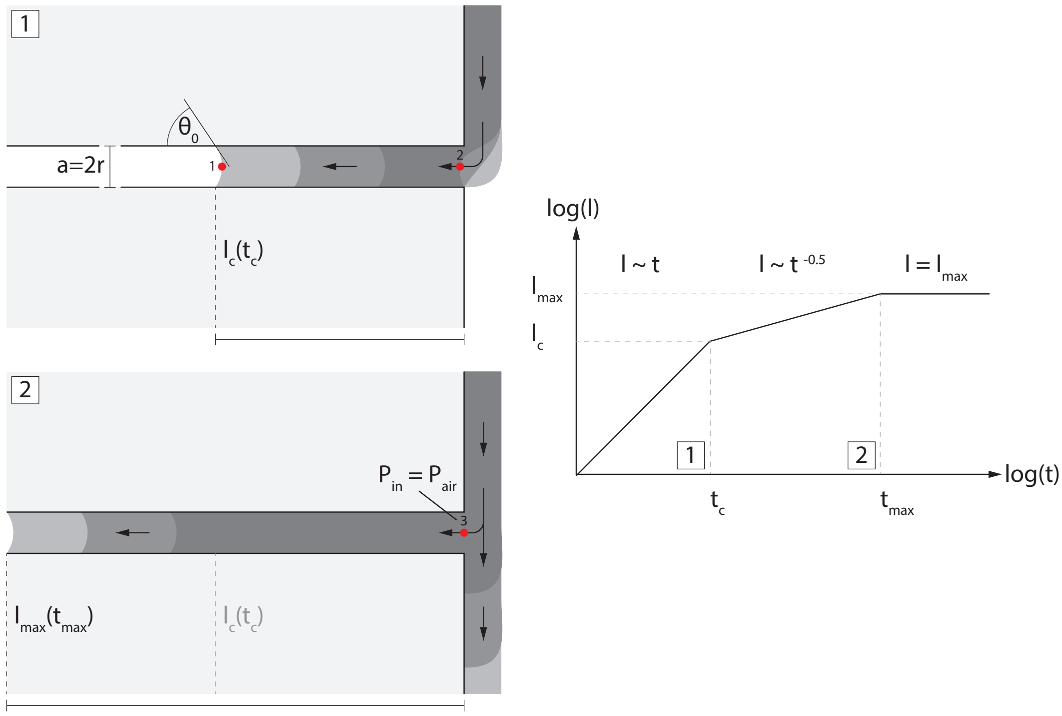

Figure 4. Conceptual model for the partitioning process at a fracture intersection. Flows on the vertical surfaces are bounded by one fracture wall only assuming wide aperture conditions. Breakthrough occurs at time t_c after which the horizontal imbibition scales as $l \sim t^{0.5}$.

3 in Fig. 4(2)). In the following analysis, we assume that partitioning occurs instantaneously at time $t = t_c$. Then, Eq. 7 can be rewritten as

$$Q_h(t) = \begin{cases} Q_0, & t \leq t_c, \\ \frac{2k\sigma\cos(\theta)}{a\mu l(t)}, & t > t_c. \end{cases} \tag{9}$$

The front position in the horizontal fracture at the time of partitioning, is obtained by setting

$$Q_0 = \frac{2k\sigma\cos(\theta)}{a\mu l_c}. \tag{10}$$

Thus, we obtain

$$l_c = \frac{2k\sigma cos(\theta)}{a\mu Q_0}. \tag{11}$$

The velocity of the displacing fluid for $t < t_c$ is equal to Q_0/a. At times t_c, the penetration depth is given by $Q_0 t_c/a = l_c$ and thus we obtain for t_c

$$t_c = \frac{l_c a}{Q_0} = \frac{2k\sigma cos(\theta)}{\mu Q_0^2}. \tag{12}$$

The penetration depth $l(t) \sim t$ increases linearly with time for $t < t_c$ and according to $l(t) \sim \sqrt{t}$ for $t > t_c$, see Appendix B. Thus, we approximate the penetration depth by matching the linear and square root behaviors at t_c as follows,

$$l(t) = \begin{cases} \frac{Q_0 t}{a}, & t \leq t_c, \\ l_c \sqrt{t/t_c}, & t > t_c. \end{cases} \tag{13}$$

Figure 5 shows l_c and t_c, computed from Eq. 11 and Eq. 12 and direct SPH simulations, as a function of the flow rate Q_{in} for three horizontal apertures (2.5, 3, and 3.5 mm). SPH simulations for the fracture aperture 2.5 mm and three different flow rates and shown in Fig. 6. In SPH simulations, we use an inter-particle spacing of $\Delta x = 5 \times 10^{-5}$ m, a density of $\rho = 1000\,\mathrm{kg\,m^{-3}}$, and a body force of $g = 9.81\,\mathrm{m\,s^{-2}}$ applied normal to the horizontal fracture plane. The surface tension is $\sigma = 0.0742\,\mathrm{kg\,s^{-2}}$ with the interaction parameters $s_{ff} = 0.015$ and $s_{sf} = 0.0125$ and speed of sound $c_0 = 3\,\mathrm{m\,s^{-1}}$. The viscosity is slightly increased to $\mu = 0.005\,\mathrm{kg\,m^{-1}s^{-1}}$ to limit the required length of the horizontal fracture (and hence computation time), which was set to $L = 0.25\,\mathrm{m}$. The no-slip boundary condition is enforced with $\beta = 25$ (see Fig. 1). For the flow rates between $Q_0 = 3 \times 10^{-5}\,\mathrm{m^2\,s^{-1}}$ and $8 \times 10^{-5}\,\mathrm{m^2\,s^{-1}}$ and fracture apertures between $a =$ 2.5 mm and 3.5 mm, the critical penetration length can be observed within the chosen fracture length. In order to avoid erratic partitioning behavior at the fracture intersections (i.e., bypassing droplets) we initiate the simulations with a rivulet on the upper vertical surface which is already in contact with the horizontal fracture aperture at the start of the simulation. While under certain conditions this may prevent other partitioning patterns (e.g. droplets, snapping rivulets) at the intersection, Noffz et al. (2018) demonstrated with laboratory experiments that this behavior is to be expected at consecutive fracture intersections. Independent of the initial flow mode (rivulets, droplet), they found that after the first fracture intersection the flow on vertical walls was dominated by rivulets. Figure 5 demonstrates that our SPH simulations are in good agreement with the analytical predictions of Eq. 11 and Eq. 12 for small fracture apertures (2.5 and 3 mm) and larger Q_0 but slightly deviate for larger apertures (3.5 mm) and smaller Q_0, resulting in the maximum error of $\sim 12\%$. We partially attribute this to the fact that contact angles θ changes during the water penetration into the horizontal fracture (e.g., (Popescu et al., 2008)). In our analytical model, we disregard dynamic variations in the contact angle and compute θ as an average of the contact angles right after the onset of fracture

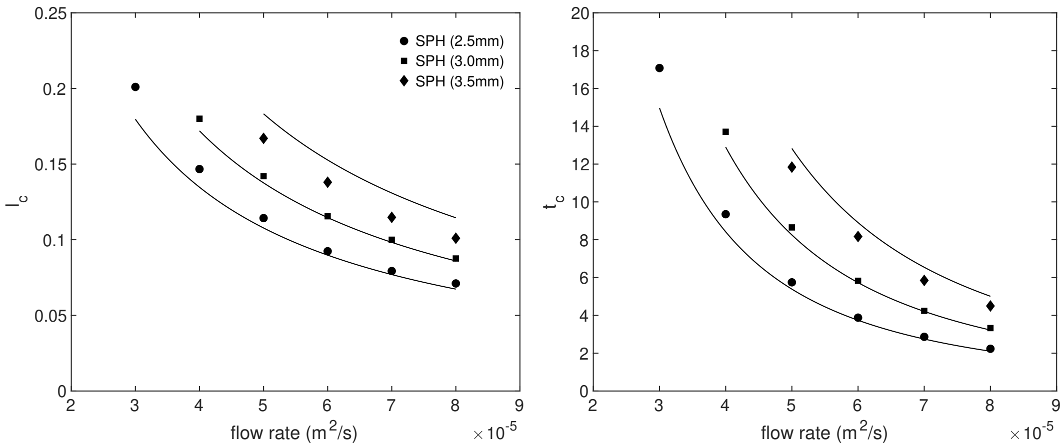

Figure 5. Critical transition times t_c and critical length l_c of the SPH model and the respective analytical solutions (black lines, Eq. 11 and 12). Contact angles are taken as averages of the angle at initial fracture penetration and the angle at t_c.

penetration and close to t_c. Yet, Fig. 5 demonstrates that our analytical solutions provide an overall good approximation of the partitioning dynamics.

3.2 Analytical solution for the transfer function

We now derive analytical solutions for the $l(t)$, the front position (or the depth of penetration) in the horizontal fracture and $Q(t)$, the outflow rate below the horizontal fracture junction where fluid is discharged.

Given that the inflow consists of (1) a linear penetration phase and (2) a Washburn-type penetration period, we obtain an analytical solution as follows

$$\frac{dl}{dt} = v_f(t) = \frac{Q_0}{a} \begin{cases} 1, & t \leq t_c, \\ \frac{1}{2}\left(\frac{t}{t_c}\right)^{-1/2}, & t_c < t < t_{max}. \end{cases} \tag{14}$$

$v_f(t)$ is the Washburn-type flow velocity after the critical time t_c and t_{max} the time at which the horizontal fracture is fully saturated and all fluid is channeled further down into the vertical fracture segment.

Figure 7 shows $l(t)$ and $dl(t)/dt$ obtained from Eq. 14 and the SPH simulations shown in Fig. 6 for an aperture $a = 2.5\,\mathrm{mm}$ and an inflow rate of $Q = 5 \times 10^{-5}\,\mathrm{m^2\,s^{-1}}$. The early time behavior is characterized by a plug-flow regime and hence $l(t) \sim t$, whereas after the critical time $t_c = 5.54\,\mathrm{s}$ the inflow scales as $l(t) \sim \sqrt{t}$ (grey lines show both scaling regimes). The analytical solution for the penetration velocity dl/dt can describe both regimes (before and after the critical time t_c) and is in very good agreement with the numerical result. A slight deviation can be observed right after the onset of the Washburn behavior at time t_c, where the channeling into the lower vertical fracture is initiated. Here, a very brief build up of fluid at the fracture intersection occurs until a critical contact angle is reached and fluid flow downwards. Figure 6 shows three partitioning types, which ultimately depend on the critical time t_c. For smaller t_c, the breakthrough process is a rather fast process ("full partitioning"), while for larger t_c, the build up of fluid on the vertical surface (see Fig. 6, left row, middle) slightly disperses the breakthrough, yet a clear sequential progression of plug flow followed by Washburn flow in the horizontal fracture can be observed. The process of fluid build up is not explicitly considered in our solution and is likely to induce the small temporary drop of the inflow velocity right after t_c. However, at later times the velocity correctly converges towards the $l(t) \sim t^{0.5}$ scaling. The cutoff at t_{max} is not shown here as the simulations are stopped when flow reaches the end of the horizontal fracture such that $dl/dt = 0$. It should be noted that for very small t_c or large Q_0, flow may not exhibit the clear dynamics of sequential partitioning and a breakthrough can occur right away even before the theoretical time t_c due to effects of inertia, which we do not consider. Yet, for the covered range of flow rates our model is in very good agreement with the theoretical solution.

In order to model the response of the system to a constant input signal Q_0 we obtain the outflow rate Q leaving the system:

$$Q = Q_0 - v_f(t)a\,. \tag{15}$$

Thus, the dimensionless flow rate is

$$F(t) = \frac{Q(t)}{Q_0} = H(t-t_c) - \frac{1}{2}\left(\frac{t}{t_c}\right)^{-1/2} \mathbb{I}(t_c < t < t_{max}). \tag{16}$$

Next, we define the normalized transfer function as

$$\varphi(t) = \frac{dF(t)}{dt}. \tag{17}$$

The transfer function for a plug flow type regime followed by a Washburn type behavior has the form

$$\begin{aligned}\varphi_{pw}(t) = \frac{dF}{dt} &= \delta(t-t_c) + \frac{1}{2}\left(\frac{t}{t_c}\right)^{-1/2}[\delta(t-t_{max}) - \delta(t-t_c)] \\ &+ \frac{1}{4t_c}\left(\frac{t}{t_c}\right)^{-3/2}, I(t_c < t < t_{max})\end{aligned} \tag{18}$$

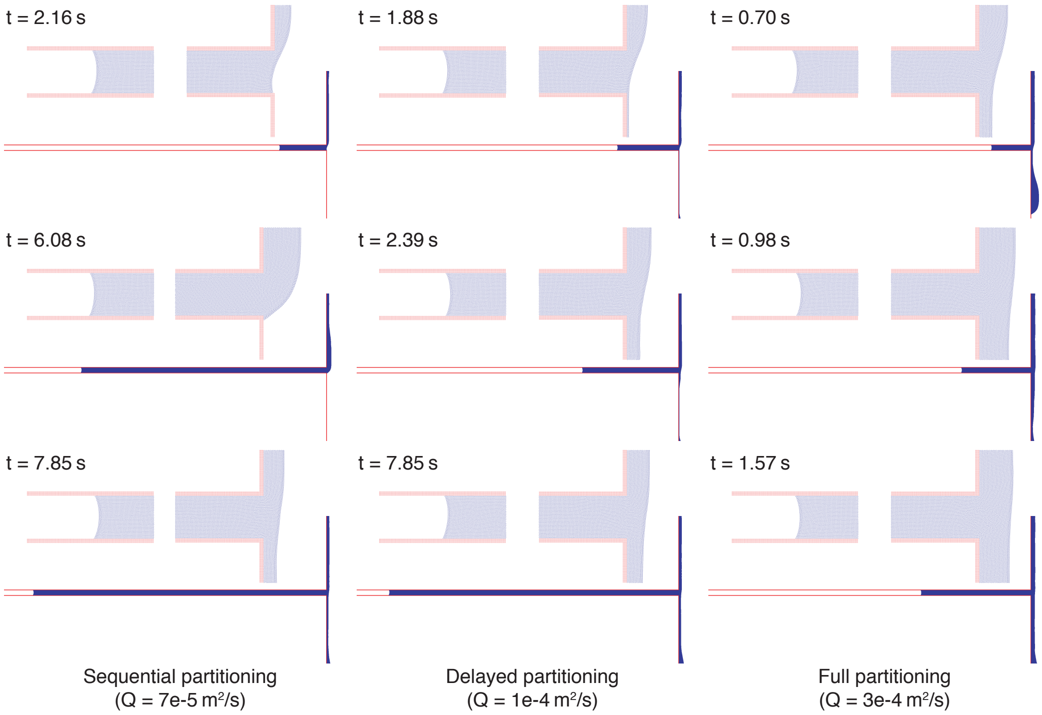

Figure 6. Partitioning regimes at the horizontal fracture intersection (shown for an aperture of $a = 2.5\,\mathrm{mm}$) for three different flow rates (increasing from left to right) and at three time steps. Three regimes can be distinguished: (1) Sequential partitioning, (2) delayed partitioning and (3) full partitioning. A detailed description of the regimes can be found in the text. The insets show the detailed view of the fluid-air interface at the invading fluid front and at the fracture intersection.

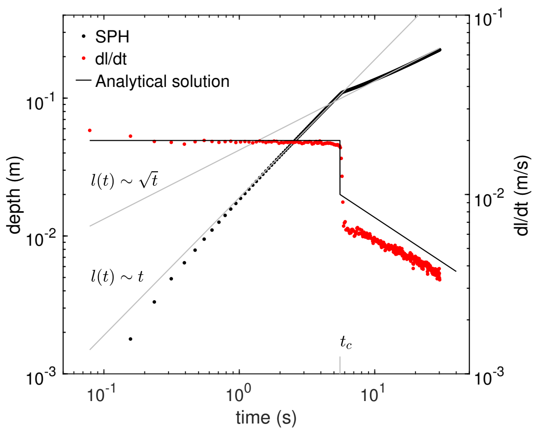

Figure 7. SPH simulations ($a = 2.5\,\mathrm{mm}$, $Q_0 = 5 \times 10^{-5}\,\mathrm{m^2\,s^{-1}}$) correctly recover the linear (plug-flow) and Washburn behavior. The inflow velocity dl/dt and the analytical solution (Eq. 14) are in very good agreement. Note that the fluid front did not fully penetrate the horizontal fracture in the simulations, hence the cutoff at t_{max} ($l = const.$, $dl/dt = 0$) is not visible here.

where δ is the Dirac delta function. In order to numerically integrate the transfer function we replace the Dirac delta function in Eq. 18 by

$$\delta \approx \delta_n(t) = \begin{cases} \frac{1}{\Delta t}, & -\frac{\Delta t}{2} < t < \frac{\Delta t}{2} \\ 0, & \text{otherwise} \end{cases} \tag{19}$$

where $\Delta t = 0.1$. Figure 8 shows the normalized outflow rate Q/Q_0 (exact and approximate solution) and its derivative, the normalized transfer function $\varphi = Q_0^{-1} dQ/dt$. The outflow Q/Q_0 is zero at first (all fluid is filling the horizontal fracture) until the critical time t_c, where partitioning sets in and inflow is characterized by a Washburn behavior. Finally, when the horizontal fracture is fully saturated at t_{max}, the outflow Q/Q_0 reaches its maximum value, i.e., $Q = Q_0$ and $Q/Q_0 = 1$.

3.3 Extension of the transfer function

In the previous section, we focused on the process of horizontal fracture inflow and partitioning, however, we did not consider the effect of additional vertical surfaces above or below the fracture intersection, which affect the system response and hence the transfer function. In the following, we extend the transfer function based on classical Nusselt film flow approximations (Nusselt, 1916), which assume a constant film thickness.

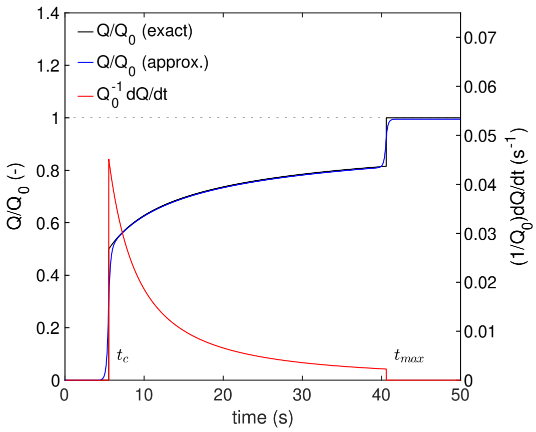

Figure 8. Normalized outflow rate and transfer function $\varphi(t) = Q_0^{-1}dQ/dt$ for a system with $a = 2.5\,\mathrm{mm}$ and $Q_0 = 5 \times 10^{-5}\,\mathrm{m}^2/\mathrm{s}$. The approximate solution for the outflow rate employs an replacement function for the Dirac function (Eq. 19).

The velocity profile of flow down an inclined plane in the x direction is governed by

$$\frac{d^2 v_x}{dy^2} = -\frac{\rho g sin(\alpha)}{\mu}, \tag{20}$$

where y is the direction normal to the surface and α is the inclination angle from the horizontal. The boundary conditions are established via a no-slip condition at $y = 0$, i.e., $v_x(0) = 0$, and the normal viscous stress being zero at the free surface $y = h$,

$$\left.\frac{dv_x}{dy}\right|_{y=h} = 0. \tag{21}$$

The solution of this problem is

$$v_x(y) = \frac{\rho g sin(\alpha)}{2\mu} y(2h - y). \tag{22}$$

The volumetric flux down the plane is then calculated as

$$Q = \int_0^h v_x dy = \frac{\rho g sin(\alpha) h^3}{3\mu} \tag{23}$$

and, hence, the maximum film height for a given Q is

$$h = \left(\frac{3\mu Q}{\rho g sin(\alpha)}\right)^{1/3}. \tag{24}$$

The depth-averaged velocity can be obtained as

$$\bar{v} = \frac{Q}{h} = \int_0^h v_x dy\,. \tag{25}$$

The effect of the upper vertical surfaces is simply a delay in the first arrival, i.e., a positive shift in the transfer function by Δt^v_{up}, given that $Q = Q_0$. Using Eq. 25 we can then simply compute Δt^v_{up} as

$$\Delta t^v_{up} = L^v_{up}\frac{h}{Q_0} = \frac{L^v_{up}}{\bar{v}_{up}} \tag{26}$$

where L^v_{up} is the total length of the upper vertical surface. On the lower vertical surface a similar shift in the transfer function is induced, however, here the outflow rate is initially $Q_c = Q(t_c)$. It should be noted that here t_c is the critical time since the beginning of the fracture penetration. For the sake of simplicity, we neglect the increase in Q after the breakthrough at t_c and assume that the flow velocity on the lower vertical surface depends on the breakthrough flow rate Q_c. The flow rate at the critical breakthrough is obtained via Eqs. 14 and 15 as

$$Q_c = Q_0 - v_c a, \tag{27}$$

where $v_c = \lim_{\epsilon\to 0} v_f(t = t_c + \epsilon)$. We then obtain the time Δt^v_{low} as

$$\Delta t^v_{low} = L^v_{low}\frac{h}{Q_c} = \frac{L^v_{low}}{\bar{v}_{low}} \tag{28}$$

and define the total shift induced by the upper and lower vertical surfaces as

$$\Delta T = \Delta t^v_{up} + \Delta t^v_{low}\,. \tag{29}$$

The cutoff at time t_{max}, when the horizontal fracture is fully saturated can be computed by setting $l(t_{max}) = l_{max}$, which gives

$$t_{max} = t_c(l_{max}/l_c)^2 \tag{30}$$

The flow rate at the cutoff time t_{max} can be evaluated using Eq. 14 with $v_{max}(t = t_{max} - \lim_{x\to\infty}\frac{1}{x})$ yielding the flow rate

$$Q_{max} = Q_0 - v_{max}a. \tag{31}$$

We are now able to compute the full transfer function including the residence times on the upper and lower vertical surfaces as well as the cutoff at full fracture saturation. In the next chapter, we extend this analysis to model discharge through arbitrary large stacks of fracture intersections via linear response theory.

3.4 Analytical percolation model for fracture cascades

Following Noffz et al. (2018), we employ the transfer function in the context of linear response theory (Jury et al., 1986) to model the outflow rate $Q_n(t)$ at the bottom of the vertical surface intersected by n horizontal fractures. The considered geometry and its properties with respect to the transformation of an input signal Q_0 serves as a proxy for consecutive routing through further fracture intersections of similar geometry. The outflow rate can be found as a convolution of the input signal

$$Q_n(t) = Q_0 \int_0^t dt_1 \varphi_{pw}(t - t_1) \int_0^{t_1} dt_2 \varphi_{pw}(t_1 - t_2) \cdots \int_0^{t_{n-1}} dt_n \varphi_{pw}(t_n), \tag{32}$$

or

$$Q_n(t) = \int_0^t \varphi_{pw}(t - t') Q_{n-1}(t') dt' \tag{33}$$

Note that for $n = 1$, the outflow rate $Q_1 = Q$ is given by Eq. 15.

Figure 9 shows an example for the computed outflow rates $Q_n(t)$ for a system of $n = 1$, 25 and 50 fractures employing Eq. 32 and the transfer function Eq. 18, i.e. $t_{max} > t_c$, with the Dirac delta approximation Eq. 19. Here, the maximum horizontal fracture length is $L_{max} = 0.3\,\mathrm{m}$, the aperture $a = 2.5\,\mathrm{mm}$, the static contact angle $\theta_0 = 69.0°$, the density $\rho = 1000\,\mathrm{kg\,m^{-3}}$, the surface tension $\sigma = 0.0742\,\mathrm{kg\,s^{-2}}$, viscosity $\mu = 0.005\,\mathrm{kg\,m^{-1}s^{-1}}$ and the inflow rate $Q_0 = 5 \times 10^{-5}\,\mathrm{m^2\,s^{-1}}$. The upper and lower vertical surface have a length of $L^v_{up} = L^v_{low} = 0.2\,\mathrm{m}$. Figure 10 shows the outflow rate for a system with $L_{max} = 0.05\,\mathrm{m}$ where flow is dominated by a plug flow behavior, i.e. $t_{max} > t_c$. As expected, the mean breakthrough velocity is higher and the maximum outflow rate Q_0 is reached faster due to the stronger dispersive effect of deeper horizontal fractures.

3.5 Arrival times and dispersion

The distribution of residence times after n horizontal fractures is defined by

$$f_n(t) = \frac{1}{Q_0}\frac{dQ_n(t)}{dt} = \int_0^t dt_1 \varphi_{pw,p}(t - t') \int_0^{t_1} dt_2 \varphi_{pw,p}(t_1 - t_2) \ldots \int_0^{t_{n-2}} dt_{n-1} \varphi_{pw,p}(t_{n-2} - t_{n-1}) \varphi_{pw,p}(t_{n-1}) \tag{34}$$

and its Laplace transform is given by

$$f^*_n(\lambda) = \varphi^*_{pm,p}(\lambda)^n. \tag{35}$$

The first and second moments of the travel time are given by

$$m_j = (-1)^j \left.\frac{d^j f^*_n(\lambda)}{d\lambda^j}\right|_{\lambda=0} \tag{36}$$

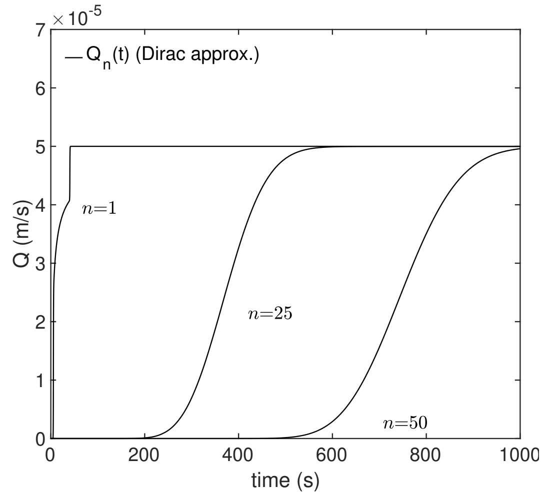

Figure 9. Application of the transfer function Eq. 18 with Eq. 19 and the convolution Eq. 32 to a system of $n = 1$, 25 and 50 fractures and $L_{max} = 0.3\,\mathrm{m}$ where $t_{max} > t_c$ (further parameters, see text). The solution takes into account the shift in time of Δt^v_{up} and Δt^v_{low}

.

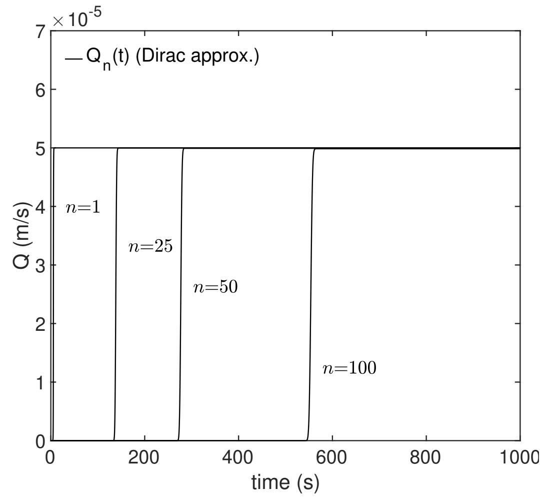

Figure 10. Application of the transfer function Eq. 18 with Eq. 19 and the convolution Eq. 32 to a system of n =1, 25, 50 and 100 fractures and $L_{max} = 0.05\,\mathrm{m}$ where $t_{max} < t_c$ (further parameters, see text). The solution takes into account the shift in time of Δt^v_{up} and Δt^v_{low}.

for $j = 1, 2$, or

$$m_1 = -\, n\varphi^*(\lambda)^{n-1}\frac{d\varphi^*(\lambda)}{d\lambda}\bigg|_{\lambda=0} \tag{37}$$

$$m_2 = n\varphi^*(\lambda)^{n-1}\frac{d^2\varphi^*(\lambda)}{d\lambda^2}\bigg|_{\lambda=0} + n(n-1)\varphi^*(\lambda)^{n-2}\left[\frac{d\varphi^*(\lambda)}{d\lambda}\right]^2\bigg|_{\lambda=0}. \tag{38}$$

Thus, for the mean and the variance of residence time we obtain

$$\begin{aligned} m_1 &= -\, n\frac{d\varphi^*(\lambda)}{d\lambda}\bigg|_{\lambda=0} \\ \sigma^2 &= n\frac{d^2\varphi^*(\lambda)}{d\lambda^2}\bigg|_{\lambda=0} - n\left[\frac{d\varphi^*(\lambda)}{d\lambda}\right]^2\bigg|_{\lambda=0}. \end{aligned} \tag{39}$$

This means that the first moment and the variance are given by

$$m_1 = nh_1, \qquad \sigma^2 = n(h_2 - h_1^2), \tag{40}$$

where h_1 and h_2 are the first and second moments of the residence time for a single fracture. They are given by (see Appendix C)

$$h_1 = t_c\left(\frac{t_{max}}{t_c}\right)^{3/2} \tag{41}$$

$$h_2 = t_c^2\left[\frac{1}{3} + \left(\frac{t_{max}}{t_c}\right)^{3/2}\right]. \tag{42}$$

In order to determine the fluid arrival times after n fractures, we add a constant time shift ΔT to the residence time in a single horizontal fracture. Thus, the quantities h_1 and h_2 are modified as

$$h_{1T} = h_1 + \Delta T \tag{43}$$

$$h_{2T} = h_2 + 2h_1\Delta T + \Delta T^2. \tag{44}$$

We non-dimensionalize time with respect to the critical time t_c such that

$$\widetilde{h}_1 = \frac{h_1}{t_c} = \tau_m^{1/2} \tag{45}$$

$$\widetilde{h}_2 = \frac{h_2}{t_c^2} = \frac{1}{3} + \frac{2}{3}\tau_m^{3/2}, \tag{46}$$

where $\tau_m = t_{max}/t_c$ is found from Eq. 30 as

$$\tau_m = (l_{max}/l_c)^2. \tag{47}$$

The arrival time moments are non-dimensionalized accordingly as

$$\widetilde{h}_{1T} = \tau_m^{1/2} + \tau_0 \tag{48}$$

$$\widetilde{h}_{2T} = \frac{1}{3} + \frac{2}{3}\tau_m^{3/2} + 2\tau_m^{1/2}\tau_0 + \tau_0^2. \tag{49}$$

where the dimensionless $\tau_0 = \Delta T/t_c$ (Eq. 12 and 29) is given by

$$\tau_0 = \frac{\Delta z}{2} \frac{[3\mu Q_0/\rho g \sin(\alpha)]^{1/3} 6\mu Q_0}{a^3 \sigma \cos(\theta)} (1 + 2^{2/3}). \tag{50}$$

The equivalent flow velocity and dispersion coefficients are given in terms of the mean m_1 and variance σ^2 of the arrival times at a plane at $z = n\Delta z$, where Δz is the spacing between horizontal fractures,

$$v = \frac{n\Delta z}{m_1} \tag{51}$$

$$D = \frac{v^3 \sigma^2}{2n\Delta z}. \tag{52}$$

We non-dimensionalize lengths by Δz and obtain

$$\widetilde{v} = \frac{1}{\widetilde{h}_{1T}} = \frac{1}{\tau_m^{1/2} + \tau_0} \tag{53}$$

$$\widetilde{D} = \frac{1}{2\widetilde{h}_{1T}^3} \left(\widetilde{h}_{2T} - \widetilde{h}_{1T}^2 \right) = \frac{\frac{1}{3} + \frac{2}{3}\tau_m^{3/2} - \tau_m}{2\left(\tau_m^{1/2} + \tau_0\right)^3}. \tag{54}$$

In the following, we study the behavior of the non-dimensional dispersion coefficient $\widetilde{D}$ and the flow velocity $\widetilde{v}$ as functions of the non-dimensional times τ_m and τ_0.

3.6 Dimensionless analysis of flow through a fracture network

To investigate the effect of non-dimensional times τ_m and τ_0 on the dimensionless flow velocity $\widetilde{v}$ and dispersion coefficient $\widetilde{D}$ (Eq. 53 and Eq. 54), we conduct a multi-parameter study. The minimum and maximum values of τ_m and τ_0 are computed for all parameter combinations of Q_0, l_{max}, θ_0, a, and Δz. We vary Q_0 in the range of 1×10^{-6} to $1 \times 10^{-2}\,\mathrm{m^2\,s^{-1}}$, which yields a maximum film thickness on the vertical surfaces of 1.5 mm according to Eq. 24. The horizontal fracture depth l_{max} ranges from 0.01 to 4 m with an aperture a of 0.5 to 10 mm. The static contact angle θ_0 is chosen to vary from 5° to 85°, i.e., corresponds to a wetting regime. Finally, the vertical fracture spacing Δz ranges from 0.1 to 25 m. For the given parameter ranges, τ_m can take values between 8.1×10^{-6} and 1.4×10^5, and τ_m between 3.2×10^{-15} and 6.46. While the above chosen parameters are within feasible ranges, we further limit the relevant range of τ_m and τ_0 by constraining the Reynolds numbers within the horizontal fracture. Here we calculate the critical Reynolds numbers as

$$Re_c = \frac{\rho v_c a}{\mu} \tag{55}$$

where the characteristic velocity v_c is computed from the critical length and time

$$v_c = \frac{l_c}{l_t} \tag{56}$$

We chose a maximum value of $Re_c = 150$ to stay within the steady non-linear laminar flow regime as for example studied by Dybbs and Edwards (1984).

Figures 11 and 12 show the non-dimensional dispersion $\widetilde{D}$ and flow velocity $\widetilde{v}$ plotted versus the dimensionless times τ_m and τ_0 over the whole chosen parameter space. The color-coded circles represent the critical Reynolds number Re_c for each parameter combination scaled from 0.1 to 150, where blue corresponds to lower values. Recall, that τ_m encodes the timescale related to the imbibition process in the horizontal fractures, and τ_0 the timescale for flow on the vertical fracture. Figure 11 (left) shows the dependence of the non-dimensional dispersion coefficient $\widetilde{D}$ on the horizontal fracture timescale τ_m for several values of the vertical fracture timescale τ_0. In general, $\widetilde{D}$ is increasing with higher values of τ_m and approaches a constant maximum of $\widetilde{D} = 0.08$ for $\tau_m > 10^5$. Within the maximum ranges defined for the Reynolds number, only values of $\tau_0 < 1$ are close to reaching this constant maximum, while for $\tau_0 > 1$, the dispersion is increasing for the considered range of τ_m. The smaller initial gradient of $\Delta\widetilde{D}/\Delta\tau_m$ (e.g., $\tau_0 = 7.5$) is caused by the non-linear Washburn dynamics within the horizontal fracture. For smaller values of τ_m, the initial rapid (potentially plug-flow type when $t_{max} < t_c$) infiltration dominates the bulk flow, while for higher values of τ_m, the classical $\sqrt{t}$ scaling comes into effect and causes stronger dispersion of the breakthrough signal. Further, this example demonstrates how the ratio of τ_m and τ_0 affects the non-dimensional dispersion coefficient. Increasing the ratio of τ_0/τ_m strengthens the dominance of the vertical flow paths and hence decreases the overall dispersion, which in our model entirely stems from the horizontal fracture imbibition. However, it should be noted that this effect is negligible for values of $\tau_0 < 10^{-5}$ (Re_c restricted) and already vanishes for $\tau_0 < 0.1$. This is similar to the behavior displayed by the dimensional example (Figs. 9 and 10), where the number of fractures and, hence, the magnitude of horizontal imbibition (inversely related to the fracture spacing Δz) is positively correlated with the dispersion and for plug-flow-regime dynamics, no dispersion occurs ($t_{max} > t_c$, equivalent to a very high ratio of τ_0/τ_m or low values of τ_m).

Figure 11 (right) demonstrates the dependence of the dimensionless flow velocity $\widetilde{v}$ on the horizontal fracture timescale τ_m for a range of τ_0 between 0 and 7.5. Two regimes can be observed. For low values of τ_m, the velocity converges towards a constant value, while for higher τ_m the non-dimensional velocity scales as $\widetilde{v} \sim \tau_m^{-1/2}$ in accordance with Eq. 53. This transition occurs at the time τ_m that increases with τ_0/τ_m due to the increased impact of vertical film flow dynamics and plug-flow type dynamics in the horizontal fracture. For $\tau_0 \leq 0.01$ the velocity scales as $\widetilde{v} \sim \tau_m^{-1/2}$ over nearly the whole range of feasible τ_m values, i.e., the average breakthrough velocities decline with increasing magnitude of the horizontal fracture imbibition (e.g., deeper or wider fractures, higher static contact angles). For even lower values of $\tau_0 < 10^{-5}$ in the Re_c-restricted range, a perfect $\widetilde{v} \sim \tau_m^{-1/2}$ scaling governs the functional relation between non-dimensional velocity and horizontal fracture imbibition timescale, and no regime transition occurs.

Next we discuss the dependence of $\widetilde{D}$ and $\widetilde{v}$ on the vertical fracture timescale τ_0. Figure 12 (left) demonstrates the limited influence of the vertical fracture timescale τ_0 on the non-dimensional dispersion. Only for extreme end-members of the parameter range beyond $\tau_0 \approx 1$, the effect of vertical fracture flow is strong enough to counteract the dispersive action of the horizontal fracture and introduces a reduction in dispersion. Yet, within critical Re_c ranges $\widetilde{D}$ is only a function of τ_m. For values of about $\tau_m > 10^3$ it converges towards the constant value of $\widetilde{D} \approx 0.08$.

Similarly, the non-dimensional velocity is independent of the vertical fracture flow timescale τ_0 within critical Re_c ranges, and is only dependent on the flow dynamics within the horizontal fracture encoded by τ_m with a $\widetilde{v} \sim \tau_m^{-1/2}$ scaling behavior. It should be noted that this scaling holds for values of $\tau_m < 1$ (see Fig. 11, right), however, here the non-dimensional dispersion is $\widetilde{D} = 0$ and flow is entirely governed by plug-flow in the horizontal fracture and film flow on the vertical surfaces.

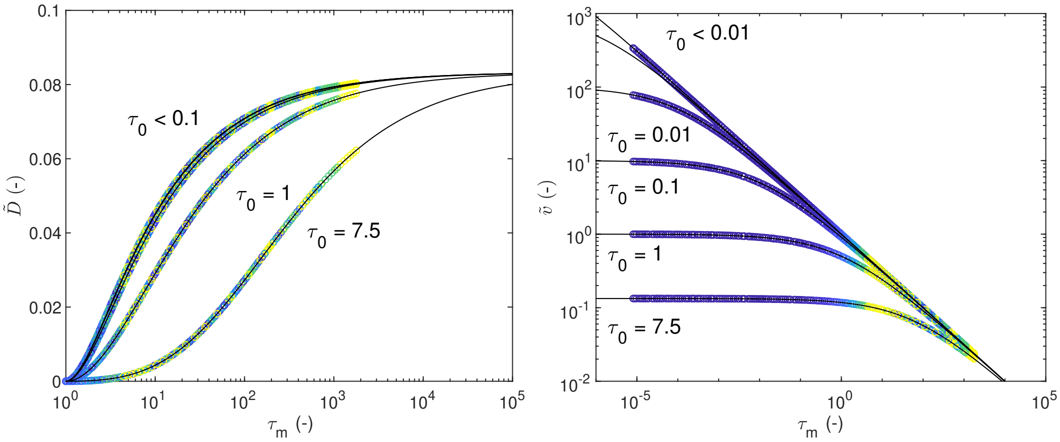

Figure 11. Non-dimensional dispersion coefficient $\widetilde{D}$ and flow velocity $\widetilde{v}$ vs. the dimensionless horizontal fracture timescale τ_m. Colored circles represent critical Reynolds numbers Re_c scaled from 0.1 (blue) to 150 (yellow). Note that $\tau_m \geq 1$ for the left plot as the the strict analytical solution for the pure plug-flow regime ($t_{max} < t_c$, $t_{max}/t_c < 1$), does not cause any type of dispersion.

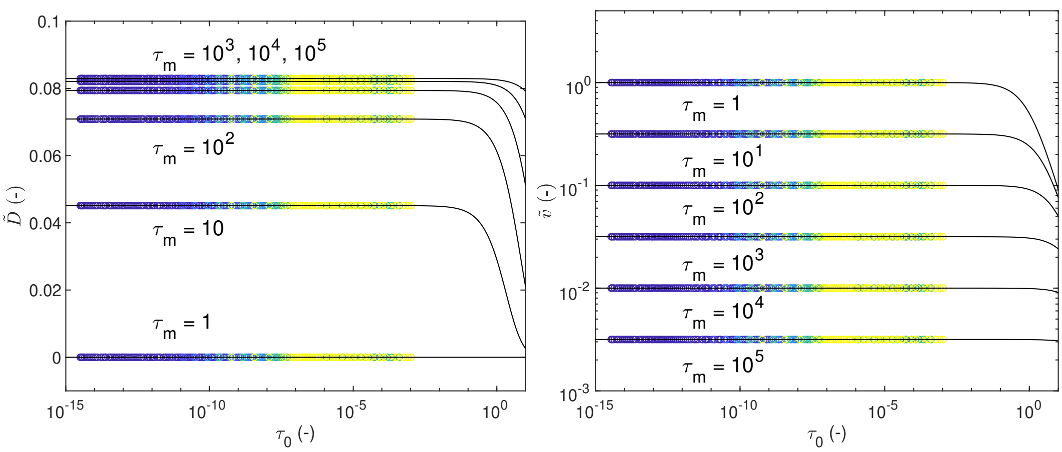

Figure 12. Non-dimensional dispersion coefficient $\widetilde{D}$ and flow velocity $\widetilde{v}$ vs. the dimensionless vertical fracture timescale τ_0. Colored circles represent critical Reynolds numbers Re_c scaled from 0.1 (blue) to 150 (yellow).

4 Conclusion and outlook

In this work, we developed an analytical solution for partially saturated flow through an arbitrary large sugar-cube type fracture network consisting of wide aperture horizontal fractures intersected by a vertical fracture. Based on numerical observations using an SPH code and former laboratory studies, we treat the partitioning dynamics at the fracture intersection as a sequential process whereby the fluid is channeled from the upper vertical surface into the horizontal fracture and finally onto the lower vertical fracture surface. Flow within the horizontal fracture is shown to follow plug-flow theory until critical pressure thresholds are exceeded. After the breakthrough, horizontal infiltration is governed by a Washburn-type scaling until the maximum horizontal fracture depth is reached and the outflow at the bottom of the system equals the inflow rate at the top. In order to model flow through arbitrary large networks of the same internal structure, we capture this process with an analytical transfer function and carry out a convolution of the constant input signal following linear response theory. Given the complex parameter space of fluid and geometric properties, we analyze the outflow dynamics in terms of non-dimensional values of τ_m and τ_0, that encode the timescales of flow in the horizontal and vertical fractures, and relate them to the non-dimensional dispersion coefficient $\widetilde{D}$ and velocity $\widetilde{v}$. It is shown that within the feasible Reynolds number range, the dimensionless dispersion coefficient converges to the values of $\widetilde{D} \approx 0.8$ with increasing τ_m and is nearly independent of τ_0, i.e., the flow in the vertical fracture does not have impact on the dispersion coefficient. Furthermore, the bulk flow velocities are characterized by a $\widetilde{v} \sim \tau_m^{-1/2}$ scaling that holds for all relevant values of τ_m and is independent of τ_0 within critical Re_c ranges.

Our work demonstrates the importance of horizontal fractures as drivers for the (lateral) dispersive action within a mainly vertically-oriented flow field. This conclusion clearly deviates from the classical piston-flow dynamics that is often assumed in the field(continuum)-scale flow models in fractured-porous systems (Lange et al., 2010; Arbel et al., 2010). Furthermore, our work sheds light on the relation between integral signals at outlet boundaries (e.g., water table fluctuations within boreholes) and the internal system geometry that transforms input signals (precipitation, recharge) and mainly contributes to its dispersion and bulk velocity within the vadose zone.

In our analysis, we simplify the infiltration process in terms of the fracture-network geometry as well as the partitioning process and flow mode occurrence. Our study assumes film flow on all vertical surfaces. This assumption is often made in studies related to preferential flow in soil systems and the respective macropore structure (Nimmo & Perkins, 2018; Nimmo, 2010, 2012; Germann et al., 2007; Bogner & Germann, 2019). However, other flow modes such as flow rate-dependent droplets (slugs) and rivulets are likely to occur on fracture surfaces (Jones et al., 2017; Dippenaar & Van Rooy, 2016; Ghezzehei & Or, 2005; Dragila & Weisbrod, 2003, 2004) and are known to affect partitioning at intersections (Xue et al., 2020; Kordilla et al., 2017; T. R. Wood et al., 2005). While droplets are more likely to bypass intersections due to their extended height (as compared to films) and hence gravitational impact (Kordilla et al., 2017), we have also demonstrated that consecutive routing of droplet flows through arrays of horizontal fractures will nearly always facilitate the formation of film (rivulet) flows on the vertical wide aperture surfaces after the first partitioning (Noffz et al., 2018). Subsequently, flow is mostly channeled into horizontal fractures without bypass, supporting the assumption of sequential flow dynamics made in this study.

As our study is limited to a two-dimensional fracture network, the observed dependence of the non-dimensional dispersion $\widetilde{D}$ and velocity $\widetilde{v}$ on the vertical and horizontal fracture flow timescales must be interpreted with care. For stable infiltration fronts, the infiltration dynamics of three-dimensional systems can be accurately recovered with two-dimensional models (e.g., Kordilla et al., 2017) using homogenization over the third dimension. However, flow on vertical fracture surfaces tends to develop instabilities even when these surfaces are perfectly smooth (Shigorina et al., 2019). Such front instabilities can contribute to fracture-specific channeling and additional dispersion. Front instabilities can develop in horizontal fractures as well, even though here the formation of instabilities is not caused by gravitational pull but is mainly a result of viscous forces and velocity variations due to changes in fracture aperture (roughness) and variations of the capillary radius (Nicholl & Glass, 2005).

In contrast to other studies, we focus on the case of vertical fractures with wide apertures. Here, the term "wide" should be interpreted with respect to the probability of fluid wetting opposing sites of the vertical fracture. For contact angles in the range of 25° to 75° droplet heights (neglecting the dynamic flattening due to movement) would be on the order of 0.75 mm to 2.4 mm, hence, setting a lower limit where one-sided flow would persist. Studies focusing on "narrow" vertical fractures often observe a slightly wider range of partitioning patterns that stem from the erratic uptake and emittance of potentially chaotic droplet patterns from T-type (Yang et al., 2019; Xue et al., 2020) and X-type intersections, (e.g., T. R. Wood et al., 2005; T. Wood & Huang, 2015; Glass et al., 2003). While the majority of fractures under common geological conditions will belong to the "narrow" category, wide aperture fractures are more likely to be found in the vadose zone where overburden pressure is limited and especially in karstic environments where fractures can be affected by dissolution (Dahan et al., 2000, 1999). As most studies are still focusing on individual intersections dynamics a unified theory for a broad range of apertures and partitioning dynamics is still to be developed.

Upscaling of individual processes, such as the intersection uptake and partitioning dynamics, remains one of the most challenging aspects in the current state of infiltration dynamics in fractured-porous media. In this work, we demonstrated how to bridge the gap between small-scale process and larger-scale bulk application by a simple convolution and the analytical derivation of (non-dimensional) dispersion and velocity parameters. In its current form, the model assumes that convolution occurs over an arbitrary number of equally structured intersections. In principle, this could be extended to sequences of intersections with dynamic properties by introducing parameter distributions that reflect changes in the transfer function φ_{pw} and hence outflow $Q_n(t)$ over the range of encountered fractures n (Eq. 32). However, while this would enhance the applicability to natural geological systems, analytical forms of $\widetilde{D}$ and $\widetilde{v}$ would be more difficult to derive. Inclusion of more complex partitioning of different flow mode dynamics, (e.g., droplets Xue et al., 2020; Yang et al., 2019) would be an interesting, yet highly challenging extension as the uptake and release of such flows at intersections introduces a highly erratic and chaotic component.

As our models assumes impermeable fracture walls, we can not model effects of porous matrix storage. This is justified for low-permeable porous systems, e.g. granites, or impermeable limestone surfaces and/or sufficiently small time scales. When considering the porous matrix, both the vertical fracture walls as well as the horizontal walls will retard the movement within the fracture, (e.g., Buscheck et al., 1991) and could be introduced via suitable storage (sink) terms into the transfer function.

In order to derive consistent and process-based infiltration functions for fractured-porous media, it is crucial to unify the various observed patterns for partitioning dynamics across the scientific community. This will require further studies on laboratory and field scales to elucidate the shortcomings of each approach and obtain a suitable array of methods adjusted for the respective study setting and data availability. Given the strong impacts of climate-change-induced transformation of precipitation patterns (Black, 2009), water resources management, specifically in arid and semi-arid regions, requires enhanced models for recharge prediction that take into account the rapid preferential flow component that may substantially contribute to groundwater replenishment under high evapotranspiration and short but extreme rainfall conditions (Pachauri et al., 2014).

5 Data availability statement

All experimental data can be downloaded from `https://data.goettingen-research-online.de/dataset.xhtml?persistentId=doi:10.25625/77DVJA`

Acknowledgments

A. Tartakovsky was supported by the U.S. Department of Energy (DOE) Office of Science, Office of Advanced Scientific Computing Research as part of the New Dimension Reduction Methods and Scalable Algorithms for Nonlinear Phenomena project.

Appendix A Smoothed Particle Hydrodynamics Model

We employ the SPH method to model free surface flow of water described by the Navier-Stokes (NS) equations, including the momentum and conservation equations

$$\frac{d\mathbf{v}}{dt} = -\frac{\nabla P}{\rho} + \frac{\mu}{\rho}\nabla^2\mathbf{v} + \mathbf{g} \qquad \nabla \cdot \mathbf{v} = 0, \tag{A1}$$

respectively, subject to the Young boundary condition at the fluid-air-solid interface, the Young-Laplace boundary condition at the water-air interface and the no-slip boundary condition at the fluid-solid interface (Kordilla et al., 2017; Tartakovsky & Panchenko, 2016; Tartakovsky & Meakin, 2005a). Here, $\mathbf{v}$ is the velocity, P the pressure, ρ the density, μ the viscosity and $\mathbf{g}$ the gravitational acceleration.

To simplify the solution of the incompressible NS equations (A1), we employ the weakly compressible formulation where the continuity equation is replaced with its compressible form $d\rho/dt = -\rho\nabla\cdot\mathbf{v}$, and the equation of state is used to close the resulting compressible NS equations:

$$P(\rho) = c_0^2\frac{\rho_0}{7}\left(\left[\frac{\rho}{\rho_0}\right]^7 - 1\right) + P_0\,, \tag{A2}$$

where ρ_0 is the reference water density, P_0 is a background pressure. The speed of sound c_0 is chosen such that $|\delta\rho|/\rho \leq 0.03$, where $|\delta\rho|$ is the maximum absolute change in density. This condition is sufficient for fluid to behave as an incompressible fluid and to obtain an accurate pressure field (Morris et al., 1997).

The SPH discretization of the weakly-compressible NS-equation is:

$$\begin{aligned}\frac{d\mathbf{v}_i}{dt} &= \sum_{j\in s+f} m_j\left(\frac{P_i}{\rho_i^2}+\frac{P_j}{\rho_j^2}\right)\hat{\mathbf{e}}_{ij}\frac{\partial W(\mathbf{r}_{ij},h)}{\partial r_{ij}} + \sum_{j\in f} m_j\frac{\mu_i+\mu_j}{\rho_i\rho_j}\frac{\mathbf{v}_{ij}}{r_{ij}}\frac{\partial W(\mathbf{r}_{ij},h)}{\partial r_{ij}} \\ &\quad + \sum_{j\in s+f}\frac{1}{m_j}\mathbf{F}_{ij}^I + \sum_{k\in s}\mathbf{F}_{ik}^B + \mathbf{g}\,,\end{aligned} \tag{A3}$$

and

$$\frac{d\rho_i}{dt} = \sum_{j=1}^{N} m_j\mathbf{v}_{ij}\cdot\hat{\mathbf{e}}_{ij}\frac{\partial W(\mathbf{r}_{ij},h)}{\partial r_{ij}}\,, \tag{A4}$$

where $\hat{\mathbf{e}}_{ij} = \mathbf{r}_{ij}/r_{ij}$ is the unit vector pointing from particle i to particle j and summations are over all fluid (f) and/or solid (s) particles and W is a two-dimensional Wendland kernel (Wendland, 1995) that establishes a smoothed interaction over the range h between particles. In order to simulate surface tension a additional pair-wise interaction term (Tartakovsky & Meakin, 2005a) is employed that consists of two overlapping cubic spline function W_1 and W_2 with a short-range repulsive and long-range attractive component controlled by coefficients A and B (Kordilla et al., 2013, 2017):

$$\mathbf{F}_{ij}^I = s\left[AW_1(r_{ij},h_1) - BW_2(r_{ij},h_2)\right]\hat{\mathbf{e}}_{ij}\,. \tag{A5}$$

The magnitude of the interaction force depends on the factor s which assumes values of s_{sf} for solid-fluid interactions and s_{ff} for fluid-fluid interactions. For values of $s_{sf} > s_{ff}$ wetting conditions are enforced, while otherwise non-wetting fluids can be simulated.

No-slip conditions are enforced via a Robin-type volumetric force term following (Pan et al., 2014)

$$\mathbf{F}_{ik}^B = \beta\mathbf{v}_i\frac{m_k}{\rho_i\rho_k}(\mathbf{n}_i+\mathbf{n}_k)\cdot\hat{\mathbf{e}}_{ij}\frac{\partial W(\mathbf{r}_{ik},h)}{\partial r_{ik}} \tag{A6}$$

where $\mathbf{n}_i$ is the normal unit vector (see the definition in (Pan et al., 2014)), $\beta = \mu/\lambda$ is the friction coefficient and λ is the artificial slip length. For most fluids, the real slip length is on the order of several nanometers, and using such a small λ would result in a prohibitively small time step in the SPH method. We demonstrate in Section 2.1, that the no-slip boundary condition can be accurately modeled by setting λ to be 100 times smaller than the domain size. We note that in Eq. A3, the summation of the viscosity term is only over fluid particles, while the no-slip condition is entirely enforced via Eq. A6. The highly non-linear form of the equation of state A2 generates sufficiently high pressure (in addition to the repulsive part of the interaction force) to prevent fluid particles from penetrating solid surfaces.

To integrate Eq. A3 a modified Velocity Verlet time-stepping scheme is employed and time steps are constraint as follows (Kordilla et al., 2017; Pan et al., 2014; Tartakovsky & Meakin, 2005c):

$$\Delta t \leq \delta \frac{h}{c}, \qquad \Delta t \leq \delta \min \sqrt{h|\mathbf{a}_i|}, \qquad \Delta t \leq \delta \min \frac{\rho_i h^2}{\mu_i}, \qquad \Delta t \leq \delta \min \frac{h(\rho_i + \rho_j)}{2\beta} \tag{A7}$$

where $\delta = 0.1$.

Appendix B Spontaneous Imbibition

The volumetric flow rate through a fracture conceptualized as a parallel plate is governed by:

$$\frac{dV}{dt} = \frac{\Delta P}{\Delta l} \frac{a^3}{12\mu} W \tag{B1}$$

,where l is the penetration depth (the length over which the pressure gradient ΔP acts), a is the aperture and W is the fracture (unit) width. The change in volume over time can be rewritten in terms of the penetration depth into the fracture

$$\frac{dV}{dt} = aW \frac{dl}{dt} \tag{B2}$$

Plugging this into Eq. B1 we obtain

$$\frac{dl}{dt} = \frac{\Delta P}{\Delta l} \frac{a^2}{12\mu} \tag{B3}$$

The capillary pressure according to Youngs law in the case of a parallel plate is

$$\Delta P_c^{2D} = \frac{\sigma cos(\theta_0)}{r} \tag{B4}$$

, where r is the radius of the fracture. Here we neglect the second principal radius which would otherwise yield, e.g. in the case of a tube geometry,

$$\Delta P_c^{3D} = \sigma cos(\theta_0)\left(\frac{1}{r_1}+\frac{1}{r_2}\right) \tag{B5}$$

Plugging this into Eq. B3 we obtain

$$\frac{dl}{dt} = \frac{\sigma cos(\theta_0)a^2}{rl(t)12\mu} = \frac{\sigma cos(\theta_0)(2r)^2}{rl(t)12\mu} = \frac{\sigma cos(\theta_0)r}{l(t)3\mu} \tag{B6}$$

Separating the variables and integration yields

$$\int_{l(t_0)}^{l} l(t)dl = \int_{t_0}^{t} \frac{\sigma cos(\theta_0)r}{3\mu}dt \tag{B7}$$

and

$$\frac{1}{2}l(t)^2 = \frac{\sigma cos(\theta_0)r}{3\mu}t + C \tag{B8}$$

such that the time-dependent penetration length becomes

$$l(t) = \left(\frac{2\sigma cos(\theta_0)r}{3\mu}t\right)^{1/2} \tag{B9}$$

Appendix C Moments

In order to calculate the moments of $\varphi_{pw}(t)$ it is advantageous to write it as follows,

$$\begin{aligned}\varphi_{pw}(t) = \frac{dF}{dt} &= \delta(t-t_c) + W(t)\left[\delta(t-t_{max}) - \delta(t-t_c)\right] \\ &- W'(t)\mathbb{I}(t_c < t < t_{max})\end{aligned} \tag{C1}$$

where we set

$$W = \frac{1}{2}\left(\frac{t}{t_c}\right)^{-1/2} \tag{C2}$$

$$W' = -\frac{1}{4t_c}\left(\frac{t}{t_c}\right)^{-3/2} \tag{C3}$$

The zeroth moment is

$$\int\limits_0^\infty dt\varphi(t) = 1 + [W(t_{max}) - W(t_c)] - [W(t_{max}) - W(t_c)] = 1. \tag{C4}$$

Now we determine the first moment:

$$\int\limits_0^\infty dtt\varphi(t) = t_c + [t_{max}W(t_{max}) - t_cW(t_c)] + \frac{\sqrt{t_c}}{4}\int\limits_{t_c}^{t_{max}} dtt^{-1/2} \tag{C5}$$

$$= t_c + [t_{max}W(t_{max}) - t_cW(t_c)] + \frac{\sqrt{t_c}}{2}(\sqrt{t_{max}} - \sqrt{t_c}) \tag{C6}$$

$$= t_c\sqrt{t_{max}/t_c} \tag{C7}$$

Now we determine the second moment:

$$\int_0^\infty dt t^2 \varphi(t) = t_c^2 + [t_{max}^2 W(t_{max}) - t_c^2 W(t_c)] + \frac{\sqrt{t_c}}{4} \int_{t_c}^{t_{max}} dt t^{1/2} \tag{C8}$$

$$= t_c^2 + [t_{max}^2 W(t_{max}) - t_c^2 W(t_c)] + \frac{\sqrt{t_c}}{6}(t_{max}^{3/2} - t_c^{3/2}) \tag{C9}$$

$$= t_c^2 \left[\frac{1}{3} + \frac{2}{3}(t_{max}/t_c)^{3/2}\right] \tag{C10}$$

References

Adler, P. M., Thovert, J. F., & Mourzenko, V. V. (2013). *Fractured Porous Media* (Vol. 9780199666). Oxford University Press. doi: 10.1093/acprof:oso/9780199666515.001.0001

Alkhatib, J., Engelhardt, I., Ribbe, L., & Sauter, M. (2019, jun). An integrated approach for choosing suitable pumping strategies for a semi-arid region in Jordan using a groundwater model coupled with analytical hierarchy techniques. *Hydrogeology Journal*, *27*(4), 1143–1157. Retrieved from `http://link.springer.com/10.1007/s10040-019-01925-0` doi: 10.1007/s10040-019-01925-0

Arbel, Y., Greenbaum, N., Lange, J., & Inbar, M. (2010). Infiltration processes and flow rates in developed karst vadose zone using tracers in cave drips. *Earth Surface Processes and Landforms*, *35*(14), 1682–1693. doi: 10.1002/esp.2010

Ascott, M. J., Gooddy, D. C., Wang, L., Stuart, M. E., Lewis, M. A., Ward, R. S., & Binley, A. M. (2017). Global patterns of nitrate storage in the vadose zone. *Nature Communications*, *8*(1), 1–6. Retrieved from `http://dx.doi.org/10.1038/s41467-017-01321-w` doi: 10.1038/s41467-017-01321-w

Ascott, M. J., Wang, L., Stuart, M. E., Ward, R. S., & Hart, A. (2016). Quantification of nitrate storage in the vadose (unsaturated) zone: a missing component of terrestrial N budgets. *Hydrological Processes*, *30*(12), 1903–1915. doi: 10.1002/hyp.10748

Barenblatt, G. I., Zheltov, I. P., & Kochina, I. N. (1960). Basic concepts in the theory of seepage of homogeneous liquids in fissured rocks [strata]. *Journal of Applied Mathematics and Mechanics*, *24*(5), 1286–1303. doi: 10.1016/0021-8928(60)90107-6

Barozzi, G. S., & Angeli, D. (2014). A note on capillary rise in tubes. *Energy Procedia*, *45*, 548–557. doi: 10.1016/j.egypro.2014.01.059

Benson, D. A. (2001). A model of water streaking down a wall. *Water Resources Research*, *37*(2), 427–430. doi: 10.1029/2000WR900309

Berkowitz, B., & Scher, H. (1995, jun). On Characterization of Anomalous Dispersion in Porous and Fractured Media. *Water Resources Research*, *31*(6), 1461–1466. Retrieved from `http://doi.wiley.com/10.1029/95WR00483` doi: 10.1029/95WR00483

Black, E. (2009, jul). The impact of climate change on daily precipitation statistics in Jordan and Israel. *Atmospheric Science Letters*, *10*(3), 192–200. Retrieved from `http://doi.wiley.com/10.1002/asl.233` doi: 10.1002/asl.233

Bodvarsson, G., Bandurraga, T., & Wu, Y. (1997). *The site-scale unsaturated zone model of Yucca Mountain, Nevada, for the viability assessment, Yucca Mountain Characterization Project Report LBNL-40376, UC-814* (Tech. Rep.). Berkeley, CA: Earth Sciences Division, Lawrence Berkeley National Laboratory.

Bogner, C., & Germann, P. (2019). Viscous Flow Approach to "Pushing Out Old Water" from Undisturbed and Repacked Soil Columns. *Vadose Zone Journal*, *18*(1), 1–10. doi: 10.2136/vzj2018.09.0168

Buscheck, T. A., Nitao, J. J., & Chesnut, D. A. (1991). The Impact of Episodic Nonequilibrium Fracture-Matrix Flow on Repository Performance at the Potential Yucca Mountain Site. *MRS Proceedings*, *257*. doi: 10.1557/proc-257-607

Chambers, L. A., Gooddy, D. C., & Binley, A. M. (2019). Use and application of CFC-11, CFC-12, CFC-113 and SF6 as environmental tracers of groundwater residence time: A review. *Geoscience Frontiers*, *10*(5), 1643–1652. Retrieved from `https://doi.org/10.1016/j.gsf.2018.02.017` doi: 10.1016/j.gsf.2018.02.017

Cook, P. G., & Solomon, D. K. (1997). Recent advances in dating young groundwater: Chlorofluorocarbons, 3H/3He and 85Kr. *Journal of Hydrology*, *191*(1-4), 245–265. doi: 10.1016/S0022-1694(96)03051-X

Dahan, O., Nativ, R., Adar, E. M., Berkowitz, B., & Ronen, Z. (1999). Field observation of flow in a fracture intersecting unsaturated chalk. *Water Resources Research*, *35*(11), 3315–3326. doi: 10.1029/1999WR900198

Dahan, O., Nativ, R., Adar, E. M., Berkowitz, B., & Weisbrod, N. (2000). *On frac-*

tured structure and preferential flow in unstaturated chalk (Vol. 38) (No. 3).

Dijk, P. E., Berkowitz, B., & Yechieli, Y. (2002). Measurement and analysis of dissolution patterns in rock fractures. *Water Resources Research*, *38*(2), 5–1–5–12. Retrieved from `http://doi.wiley.com/10.1029/2001WR000246` doi: 10.1029/2001WR000246

Dippenaar, M. A., & Van Rooy, J. L. (2016). On the cubic law and variably saturated flow through discrete open rough-walled discontinuities. *International Journal of Rock Mechanics and Mining Sciences*, *89*(December 2015), 200–211. Retrieved from `http://dx.doi.org/10.1016/j.ijrmms.2016.09.011` doi: 10.1016/j.ijrmms.2016.09.011

Dragila, M. I., & Weisbrod, N. (2003). Parameters affecting maximum fluid transport in large aperture fractures. *Advances in Water Resources*, *26*(12), 1219–1228. doi: 10.1016/j.advwatres.2003.09.002

Dragila, M. I., & Weisbrod, N. (2004). Fluid motion through an unsaturated fracture junction. *Water Resources Research*, *40*(2), 1–11. doi: 10.1029/2003WR002588

Dragila, M. I., & Wheatcraft, S. (2001). Free Surface Films. In *Conceptual models of flow and transport in the fractured vadose zone* (pp. 217–241). National Academies Press.

Dvory, N. Z., Livshitz, Y., Kuznetsov, M., Adar, E., & Yakirevich, A. (2016). The effect of hydrogeological conditions on variability and dynamic of groundwater recharge in a carbonate aquifer at local scale. *Journal of Hydrology*, *535*, 480–494. Retrieved from `http://dx.doi.org/10.1016/j.jhydrol.2016.02.011` doi: 10.1016/j.jhydrol.2016.02.011

Dybbs, A., & Edwards, R. (1984). A new look at porous media fluid mechanics—Darcy to turbulent. In *Fundamentals of transport phenomena in porous media* (pp. 199–256). Springer.

Ebel, B. A., & Nimmo, J. R. (2013). An Alternative Process Model of Preferential Contaminant Travel Times in the Unsaturated Zone: Application to Rainier Mesa and Shoshone Mountain, Nevada. *Environmental Modeling and Assessment*, *18*(3), 345–363. doi: 10.1007/s10666-012-9349-8

El-Hakim, M., & Bakalowicz, M. (2007, feb). Significance and origin of very large regulating power of some karst aquifers in the Middle East. Implication on karst aquifer classification. *Journal of Hydrology*, *333*(2-4), 329–339. Retrieved from https://linkinghub.elsevier.com/retrieve/pii/S0022169406004768 doi: 10.1016/j.jhydrol.2006.09.003

Engelhardt, I., Rausch, R., Lang, U., Al-Saud, M., & Schüth, C. (2013). Impact of Preboreal to Subatlantic shifts in climate on groundwater resources on the Arabian Peninsula. *Environmental Earth Sciences*, *69*(2), 557–570. doi: 10.1007/s12665-013-2362-7

Flint, A. L., Flint, L. E., Bodvarsson, G. S., Kwicklis, E. M., & Fabryka-Martin, J. (2001). Development of the conceptual model of unsaturated zone hydrology at Yucca Mountain, Nevada. *Conceptual Models of Flow and Transport in the Fractured Vadose Zone*, *247*, 47–85\n374. doi: 10.1016/S0022-1694(01)00358-4

Ford, D., & Williams, P. (2013). *Karst Hydrogeology and Geomorphology.* John Wiley \& Sons. doi: 10.1002/9781118684986

Germann, P. F., Helbling, A., & Vadilonga, T. (2007). Rivulet Approach to Rates of Preferential Infiltration. *Vadose Zone Journal*, *6*(2), 207. Retrieved from https://www.soils.org/publications/vzj/abstracts/6/2/207 doi: 10.2136/vzj2006.0115

Ghezzehei, T. A. (2004). Constraints for flow regimes on smooth fracture surfaces. *Water Resources Research*, *40*(11). doi: 10.1029/2004WR003164

Ghezzehei, T. A., & Or, D. (2005). Liquid fragmentation and intermittent flow regimes in unsaturated fractured media. *Water Resources Research*, *41*(12), 1–10. doi: 10.1029/2004WR003834

Glass, R. J., Nicholl, M. J., Rajaram, H., & Wood, T. R. (2003). Unsaturated flow through fracture networks: Evolution of liquid phase structure, dynamics, and the critical importance of fracture intersections. *Water Resources Research*, *39*(12), 1–12. doi: 10.1029/2003WR002015

Gunn, J. (1981). Limestone solution rates and processes in the Waitomo District, New Zealand. *Earth Surface Processes and Landforms*, *6*(5), 427–445. doi: 10.1002/esp.3290060504

Hayden, K. M., Telyakovskiy, A. S., & Wheatcraft, S. W. (2012). A note on free-surface films in fractures. *Advances in Water Resources*, *49*, 72–75. Retrieved from http://dx.doi.org/10.1016/j.advwatres.2012.06.012 doi: 10.1016/

j.advwatres.2012.06.012

Heppner, C. S., Nimmo, J. R., Folmar, G. J., Gburek, W. J., & Risser, D. W. (2007). Multiple-methods investigation of recharge at a humid-region fractured rock site, Pennsylvania, USA. *Hydrogeology Journal*, *15*(5), 915–927. doi: 10.1007/s10040-006-0149-6

Huang, H., Meakin, P., & Liu, M. (2005). Computer simulation of two-phase immiscible fluid motion in unsaturated complex fractures using a volume of fluid method. *Water Resources Research*, *41*(12), 1–12. doi: 10.1029/2005WR004204

Hussain, S. I., Frey, S. K., Blowes, D. W., Ptacek, C. J., Wilson, D., Mayer, K. U., ... Lapen, D. R. (2019). Reactive transport of manure-derived nitrogen in the vadose zone: Consideration of macropore connectivity to subsurface receptors. *Vadose Zone Journal*, *18*(1), 2–18. doi: 10.2136/vzj2019.01.0002

Jarvis, N. (1998). Modeling the impact of preferential flow on nonpoint source pollution. In H. Selim & L. Ma (Eds.), *Physical nonequilibrium in soils: modeling and application* (pp. 195—-221). Ann Arbor Press Chelsea.

Ji, S. H., Nicholl, M. J., Glass, R. J., & Lee, K. K. (2004). Influence of a simple fracture intersection on density-driven immiscible flow: Wetting vs. nonwetting flows. *Geophysical Research Letters*, *31*(14), 10–13. doi: 10.1029/2004GL020045

Ji, S.-H., Nicholl, M. J., Glass, R. J., & Lee, K.-K. (2006). Influence of simple fracture intersections with differing aperture on density-driven immiscible flow: Wetting versus nonwetting flows. *Water Resources Research*, *42*(10), 1–10. Retrieved from `http://doi.wiley.com/10.1029/2006WR004953` doi: 10.1029/2006WR004953

Jones, B. R., Brouwers, L. B., Van Tonder, W. D., & Dippenaar, M. A. (2017). Assessing geotechnical centrifuge modelling in addressing variably saturated flow in soil and fractured rock. *Environmental Science and Pollution Research*, *24*(15), 13203–13223. doi: 10.1007/s11356-016-8333-2

Jurin, J. (1718). An account of some experiments shown before the Royal Society; with an enquiry into the cause of some of the ascent and suspension of water in capillary tubes. *Philosophical Transactions of the Royal Society of London*, *30*, 739–747.

Jury, W. A., Sposito, G., & White, R. E. (1986, feb). A Transfer Function Model of Solute Transport Through Soil: 1. Fundamental Concepts. *Water Resources Research*, *22*(2), 243–247. Retrieved from `http://doi.wiley.com/10.1029/WR022i002p00243` doi: 10.1029/WR022i002p00243

Kordilla, J., Noffz, T., Dentz, M., Geyer, T., & Tartakovsky, A. M. (2017). Effect of Unsaturated Flow Modes on Partitioning Dynamics of Gravity-Driven Flow at a Simple Fracture Intersection: Laboratory Study and Three-Dimensional Smoothed Particle Hydrodynamics Simulations. *Water Resources Research*, *53*(11), 9496–9518. doi: 10.1002/2016WR020236

Kordilla, J., Sauter, M., Reimann, T., & Geyer, T. (2012). Simulation of saturated and unsaturated flow in karst systems at catchment scale using a double continuum approach. *Hydrology and Earth System Sciences*, *16*(10), 3909–3923. doi: 10.5194/hess-16-3909-2012

Kordilla, J., Tartakovsky, A. M., & Geyer, T. (2013). Advances in Water Resources A smoothed particle hydrodynamics model for droplet and film flow on smooth and rough fracture surfaces. *Advances in Water Resources*, *59*, 1–14. Retrieved from `http://dx.doi.org/10.1016/j.advwatres.2013.04.009` doi: 10.1016/j.advwatres.2013.04.009

Kurtzman, D., Shapira, R. H., Bar-Tal, A., Fine, P., & Russo, D. (2013). Nitrate fluxes to groundwater under citrus orchards in a Mediterranean climate: Observations, calibrated models, simulations and agro-hydrological conclusions. *Journal of Contaminant Hydrology*, *151*(3), 93–104. Retrieved from `http://dx.doi.org/10.1016/j.jconhyd.2013.05.004` doi: 10.1016/j.jconhyd.2013.05.004

Lange, J., Arbel, Y., Grodek, T., & Greenbaum, N. (2010). Water percolation process studies in a Mediterranean karst area. *Hydrological Processes*, *24*(13), 1866–1879. doi: 10.1002/hyp.7624

LaViolette, R. A., Glass, R. J., Wood, T. R., McJunkin, T. R., Noah, K. S., Podgorney, R. K., ... Stoner, D. L. (2003). Convergent flow observed in a laboratory-scale unsaturated fracture system ¹. *Geophysical Research Letters*, *30*(2), 10–12. Retrieved from `http://doi.wiley.com/10.1029/2002GL015775` doi: 10.1029/2002GL015775

Legait, B., & de Gennes, P.-G. (1984). Capillary rise between closely spaced plates

: effect of Van der Waals forces. *Journal de Physique Lettres*, *45*(13), 647–652. doi: 10.1051/jphyslet:019840045013064700

Liu, H. H., Salve, R., Wang, J. S., Bodvarsson, G. S., & Hudson, D. (2004). Field investigation into unsaturated flow and transport in a fault: Model analyses. *Journal of Contaminant Hydrology*, *74*(1-4), 39–59. doi: 10.1016/j.jconhyd.2004.02.004

Liu, M., Meakin, P., & Huang, H. (2007). Dissipative particle dynamics simulation of multiphase fluid flow in microchannels and microchannel networks. *Physics of Fluids*, *19*(3), 1–11. doi: 10.1063/1.2717182

Morris, J., Fox, P. J., & Zhu, Y. (1997). Modeling Low {Reynolds} Number Incompressible Flows Using {SPH}. *J. Comput. Phys.*, *136*(1), 214–226. doi: 10.1006/jcph.1997.5776

Neslon, R. (2001). *Geologic Analysis of Naturally Fractured Reservoirs*. Elsevier. doi: 10.1016/b978-0-88415-317-7.x5000-3

Nicholl, M. J., & Glass, R. J. (2005). Infiltration into an Analog Fracture. *Vadose Zone Journal*, *4*(4), 1123. Retrieved from `https://www.soils.org/publications/vzj/abstracts/4/4/1123` doi: 10.2136/vzj2004.0110

Nimmo, J. R. (2010). Theory for Source-Responsive and Free-Surface Film Modeling of Unsaturated Flow. *Vadose Zone Journal*, *9*(2), 295. doi: 10.2136/vzj2009.0085

Nimmo, J. R. (2012). Preferential flow occurs in unsaturated conditions. *Hydrological Processes*, *26*(5), 786–789. doi: 10.1002/hyp.8380

Nimmo, J. R., & Perkins, K. S. (2018). Episodic Master Recession Evaluation of Groundwater and Streamflow Hydrographs for Water-Resource Estimation. *Vadose Zone Journal*, *17*(1), 180050. doi: 10.2136/vzj2018.03.0050

Noffz, T., Dentz, M., & Kordilla, J. (2018). Analogue fracture experiments and analytical modeling of unsaturated percolation dynamics in fracture cascades. *Vadose Zone Journal*. doi: 10.2136/vzj2018.08.0155

Nusselt, W. (1916). Die Oberflächenkondensation des Wasserdampfes. *VDI-Zeitschriften*, *60*(27).

Pachauri, R. K., Allen, M. R., Barros, V. R., Broome, J., Cramer, W., Christ, R., … Dasgupta, P. (2014). *Climate change 2014: synthesis report. Contribution of Working Groups I, II and III to the fifth assessment report of the Inter-*

governmental Panel on Climate Change. Cambridge: Cambridge University Press.

Pan, W., Bao, J., & Tartakovsky, A. M. (2014). Smoothed particle hydrodynamics continuous boundary force method for Navier-Stokes equations subject to a Robin boundary condition. *Journal of Computational Physics*, *259*, 242–259. doi: 10.1016/j.jcp.2013.12.014

Popescu, M. N., Ralston, J., & Sedev, R. (2008). Capillary Rise with Velocity-Dependent Dynamic Contact Angle. *Langmuir*, *24*, 12710–12716. doi: 10.1021/la801753t

Pratt, V. (1987). Direct least-squares fitting of algebraic surfaces. In *Proceedings of the 14th annual conference on computer graphics and interactive techniques - siggraph '87* (pp. 145–152). New York, New York, USA: ACM Press. Retrieved from `http://portal.acm.org/citation.cfm?doid=37401.37420` doi: 10.1145/37401.37420

Rossman, N. R., Zlotnik, V. A., Rowe, C. M., & Szilagyi, J. (2014). Vadose zone lag time and potential 21st century climate change effects on spatially distributed groundwater recharge in the semi-arid Nebraska Sand Hills. *Journal of Hydrology*, *519*(PA), 656–669. Retrieved from `http://dx.doi.org/10.1016/j.jhydrol.2014.07.057` doi: 10.1016/j.jhydrol.2014.07.057

Sauter, M. (1992). *Quantification and Forecasting of Regional Groundwater Flow and Transport in a Karst Aquifer (Gallusquelle, Malm, SW. Germany). Dissertation* (Vol. C13).

Scanlon, B. R., & Cook, P. G. (2002). Theme issue on groundwater recharge. *Hydrogeology Journal*, *10*(1), 3–4. doi: 10.1007/s10040-001-0175-3

Scanlon, B. R., Keese, K. E., Flint, A. L., Flint, L. E., Gaye, C. B., Edmunds, W. M., & Simmers, I. (2006, oct). Global synthesis of groundwater recharge in semiarid and arid regions. *Hydrological Processes*, *20*(15), 3335–3370. doi: 10.1002/hyp.6335

Shigorina, E., Tartakovsky, A. M., & Kordilla, J. (2019). Investigation of gravity-driven infiltration instabilities in smooth and rough fractures using a pairwise-force smoothed particle hydrodynamics model. *Vadose Zone Journal*, *18*(1). doi: 10.2136/vzj2018.08.0159

Sigalotti, L., Klapp, J., Sira, E., Melean, Y., & Hasmy, A. (2003). SPH simulations of time-dependent Poiseuille flow at low Reynolds numbers. *Journal of Computational Physics*, *191*(2), 622–638. doi: 10.1016/S0021-9991(03)00343-7

Singhal, B., & Gupta, R. (2010). *Applied Hydrogeology of Fractured Rocks.* Springer Science \& Business Media.

Su, G. W., Geller, J. T., Pruess, K., & Hunt, J. R. (2001). Solute transport along preferential flow paths in unsaturated fractures. *Water Resources Research*, *37*(10), 2481–2491. doi: 10.1029/2000WR000093

Tartakovsky, A. M., & Meakin, P. (2005a). Modeling of surface tension and contact angles with smoothed particle hydrodynamics. *Physical Review E - Statistical, Nonlinear, and Soft Matter Physics*, *72*(2), 1–9. doi: 10.1103/PhysRevE.72.026301

Tartakovsky, A. M., & Meakin, P. (2005b). Simulation of Unsaturated Flow in Complex Fractures Using Smoothed Particle Hydrodynamics. *Vadose Zone Journal*, *4*(3), 848. Retrieved from `https://www.soils.org/publications/vzj/abstracts/4/3/0848` doi: 10.2136/vzj2004.0178

Tartakovsky, A. M., & Meakin, P. (2005c). A smoothed particle hydrodynamics model for miscible flow in three-dimensional fractures and the two-dimensional Rayleigh-Taylor instability. *Journal of Computational Physics*, *207*(2), 610–624. doi: 10.1016/j.jcp.2005.02.001

Tartakovsky, A. M., & Panchenko, A. (2016). Pairwise Force Smoothed Particle Hydrodynamics model for multiphase flow: Surface tension and contact line dynamics. *Journal of Computational Physics*, *305*, 1119–1146. Retrieved from `http://dx.doi.org/10.1016/j.jcp.2015.08.037` doi: 10.1016/j.jcp.2015.08.037

Tokunaga, T. K. (2009). Hydraulic properties of adsorbed water films in unsaturated porous media. *eScholarship University of California*.

Tokunaga, T. K., & Wan, J. M. (1997). Water Film Flow Along Fracture Surfaces of Porous \t\t\t Rock. *Water Resour. Res.*, *33*(6), 1287–1295. Retrieved from `http://dx.doi.org/10.1029/97WR00473{\%}5Cnhttp://www.agu.org/journals/wr/v033/i006/97WR00473/97WR00473.pdf` doi: 10.1029/97wr00473

Tokunaga, T. K., & Wan, J. M. (2001). Surface-zone flow along unsaturated rock fractures. *Water Resources Research*, *37*(2), 287–296. doi:

10.1029/2000WR900242

Tsang, C.-F., Neretnieks, I., & Tsang, Y. (2015). Hydrologic issues associated with nuclear waste repositories. *Water Resources Research*, *51*(9), 6923–6972. Retrieved from `http://doi.wiley.com/10.1002/2015WR017641` doi: 10.1002/2015WR017641

Wang, L., Butcher, A. S., Stuart, M. E., Gooddy, D. C., & Bloomfield, J. P. (2013). The nitrate time bomb: A numerical way to investigate nitrate storage and lag time in the unsaturated zone. *Environmental Geochemistry and Health*, *35*(5), 667–681. doi: 10.1007/s10653-013-9550-y

Weisbrod, N., Nativ, R., Adar, E, M., & Ronen, D. (2000). Salt accumulation and flushing in unsaturated fractures in an arid environment. *Ground Water*, *38*(3), 452.

Wendland, H. (1995). Piecewise polynomial, positive definite and compactly supported radial functions of minimal degree. *Advances in Computational Mathematics*, *4*(1), 389–396. doi: 10.1007/BF02123482

Williams, P. W. (2008). The role of the epikarst in karst and cave hydrogeology: A review. *International Journal of Speleology*, *37*(1), 1–10. doi: 10.5038/1827-806X.37.1.1

Wood, T., & Huang, H. (2015). Experimental and Modeling Studies of Episodic Air-Water Two-Phase Flow in Fractures and Fracture Networks. In *Fluid dynamics in complex fractured-porous systems.* Wiley.

Wood, T. R., Nicholl, M. J., & Glass, R. J. (2002). Fracture intersections as integrators for unsaturated flow. *Geophysical Research Letters*, *29*(24), 44–1–44–4. Retrieved from `http://doi.wiley.com/10.1029/2002GL015551` doi: 10.1029/2002GL015551

Wood, T. R., Nicholl, M. J., & Glass, R. J. (2005). Influence of fracture intersections under unsaturated, low-flow conditions. *Water Resources Research*, *41*(4), 1–17. doi: 10.1029/2004WR003281

Xue, S., Yang, Z., Hu, R., & Chen, Y. (2020). Splitting Dynamics of Liquid Slugs at a T-Junction. *Water Resources Research*, *56*(8), 1–17. doi: 10.1029/2020wr027730

Yang, Z., Xue, S., Zheng, X., & Chen, Y. (2019, aug). Partitioning Dynamics of Gravity-Driven Unsaturated Flow Through Simple T-Shaped Fracture Intersections. *Water Resources Research*, *55*(8), 7130–7142. Retrieved from https://onlinelibrary.wiley.com/doi/abs/10.1029/2018WR024349 doi: 10.1029/2018WR024349

Zhou, Q., Salve, R., Liu, H. H., Wang, J. S., & Hudson, D. (2006). Analysis of a mesoscale infiltration and water seepage test in unsaturated fractured rock: Spatial variabilities and discrete fracture patterns. *Journal of Contaminant Hydrology*, *87*(1-2), 96–122. doi: 10.1016/j.jconhyd.2006.05.001